

1 Dissolved oxygen budget in the Levantine Sea: a coupled 2 physical-biogeochemical modelling approach

3 Joelle Habib^{1,2,3}, Caroline Ulses¹, Claude Estournel¹, Milad Fakhri³, Patrick Marsaleix¹, Thierry Moutin⁴, Dominique
4 Lefevre⁴, Mireille Pujo-Pay⁵, Marine Fourier², Laurent Coppola^{2,6}, Cathy Wimart-Rousseau⁷ and Pascal Conan^{5,6*}

5 ¹Laboratoire d'Etudes en Géophysique et Océanographie Spatiales (LEGOS), Université de Toulouse,
6 CNES/CNRS/IRD/UT3, 14 avenue Edouard Belin, 31400 Toulouse, France

7 ²Sorbonne Université, CNRS, Laboratoire d'Océanographie de Villefranche, LOV, 06230 Villefranche-sur-Mer,
8 France

9 ³National Center for Marine Sciences, National Council for Scientific Research (CNRS-L), Jounieh, Lebanon

10 ⁴Aix Marseille Université, CNRS, Université de Toulon, IRD, OSU Pythéas, Mediterranean Institute of Oceanography
11 (MIO), UM 110, 13288, Marseille, France

12 ⁵Sorbonne Université, CNRS, Laboratoire d'Océanographie Microbienne, LOMIC, F-66650 Banyuls-sur-Mer, France
13 France

14 ⁶Sorbonne Université, CNRS OSU STAMAR – UAR2017, 4 Place Jussieu, 75252 Paris, France

15 ⁷National Oceanography Centre Southampton, European Way, Southampton, SO14 3ZH, UK

16 * Deceased

17 *Correspondence to:* Joelle Habib (joellehabib22@hotmail.com)

18 **Abstract.**

19 The Levantine Basin is an ultra-oligotrophic region and the formation site of Levantine Intermediate Water. A high-
20 resolution 3D coupled hydrodynamic-biogeochemical model (SYMPHONIE-Eco3MS) was used to investigate the
21 seasonal and interannual variability of dissolved oxygen (O₂) in the Levantine Basin and to estimate its basin-wide
22 budget over the period 2013–2020. The model results show a pronounced seasonal cycle of air-sea exchanges. During
23 winter, cooling and vertical mixing induce an undersaturation in oxygen of the surface layer by up to 2% across the
24 entire basin, leading to atmospheric oxygen absorption. In contrast, during the stratified period, primary production
25 and warming induce a slight oversaturation and subsequent oxygen release to the atmosphere. The annual budget over
26 the 7-year period shows that the basin acts as a net sink for atmospheric oxygen. The oxygen budget analyses further
27 indicate that the surface layer (0-150m) acts as a source of dissolved oxygen for intermediate depths through winter
28 vertical export, whose amplitude is significantly governed by the magnitude of heat fluxes. At the basin and annual
29 scale, we estimate a net lateral oxygen input into the basin from the Ionian Sea and a net export towards the Aegean
30 Sea, with this lateral export at both surface and intermediate layers enhanced when winter heat loss is intense.
31 Biogeochemically, the Levantine Basin alternates between autotrophic and heterotrophic states on an annual basis,
32 depending on the intensity of winter surface heat loss. Spatially, the Rhodes Gyre, a quasi-permanent cyclonic
33 structure and major site of intermediate water formation, emerges as a significant oxygen pump in winter, with annual
34 uptake rates twice as high as the rest of the Levantine Basin, and shows enhanced biological production during the

35 productive season, contributing to 41% of the net annual oxygen production in the surface layer in the basin. This
36 study highlights the need for further modeling studies on pluri-annual and multi-decadal scales to explore interannual
37 variability and evolution of the annual oxygen budget across the entire Eastern Basin, particularly in the context of
38 climate change.

39 **1 Introduction**

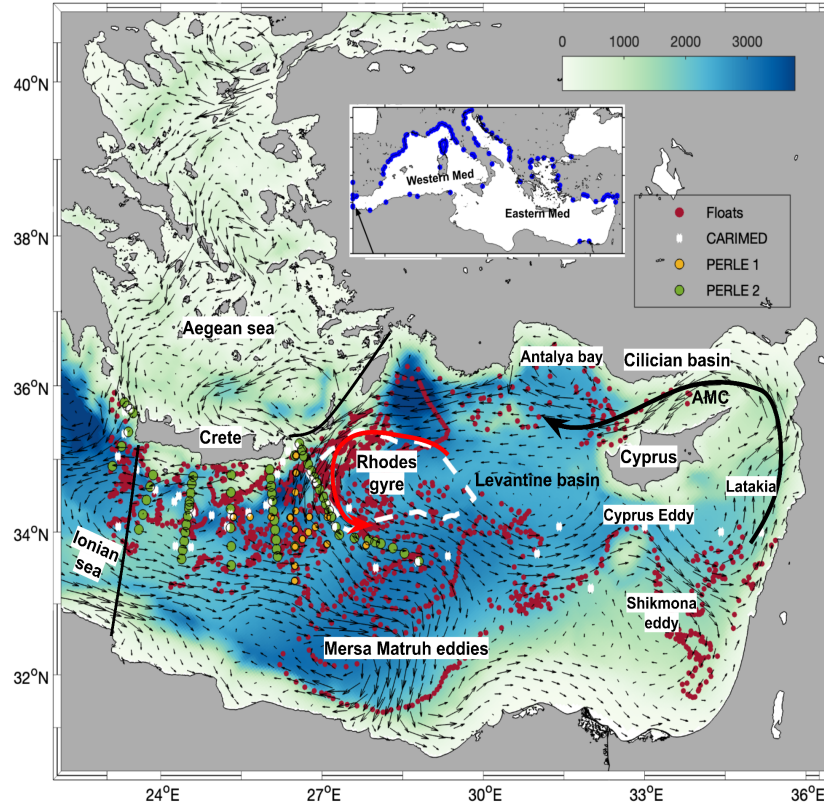
40 Dissolved oxygen (O₂) is essential for marine life, supporting respiration of living organisms and the oxidation of
41 organic matter, thereby regulating nutrient cycling and organic matter remineralization, and influencing the
42 biogeochemical cycles of important elements in the ocean (Breitburg et al., 2018; Gruber, 2011; Morée et al., 2023).
43 The ocean's oxygen inventory is primarily controlled by its production through photosynthesis, and its consumption
44 through remineralization, as well as by temperature and salinity-dependent oxygen solubility, air-sea exchange and
45 the mixing and advective fluxes influencing the ventilation of water masses (Sanders et al. 2026; Helm et al, 2011).
46 Since 1960, the total oxygen inventory has decreased by 2% in the Global Ocean (Schmidtko et al., 2017), a decline
47 primarily attributed to warming-induced reductions in oxygen solubility and to enhanced upper-ocean stratification,
48 which limits vertical ventilation (Helm et al., 2011; Schmidtko et al., 2017; Breitburg et al., 2018; Stramma and
49 Schmidtko, 2021). However, oxygen changes present large regional and temporal heterogeneity (Schmidtko et al.,
50 2017; Levin, 2018, Feucher et al., 2022; Kolodziejczyk et al., 2024; Wu et al, 2025), making long-term trends difficult
51 to detect in the upper ocean. Identifying the relative contribution of physical and biogeochemical drivers is therefore
52 essential to better understand regional oxygen dynamics.

53 The Levantine Basin, in the south-easternmost Mediterranean Sea (Fig. 1) is an ultra-oligotrophic region characterized
54 by exceptionally low primary productivity (Kress and Herut, 2001) and is particularly sensitive to changes in
55 ventilation and biogeochemical processes. As the area of the formation of the Levantine Intermediate Water (LIW)
56 which subsequently supplies the Eastern Intermediate Water (EIW), propagating throughout the entire Mediterranean
57 Sea at intermediate depths (Brasseur et al., 1996), the Levantine Basin plays a crucial role in basin-scale ventilation
58 (Kress et al., 2003). Its vertical structure of dissolved oxygen reflects the complex interplay of physical, biological,
59 and chemical processes occurring at several temporal and spatial scales. The surface and intermediate waters
60 characterized by exchanges with the atmosphere are well oxygenated, with a pronounced ventilation in the Rhodes
61 Gyre, a permanent cyclone in the northwest of the basin, which has traditionally been identified as the major area of
62 LIW formation (Lascaratos et al., 1999; Lascaratos and Nittis, 1998; Sur et al., 1993). The upper layer (0-150m)
63 exhibits seasonal variability, with maximum oxygen values located in the mixed layer in winter, while during the
64 stratification period, a subsurface oxygen maximum layer develops near 80 m depth, mostly attributed to both physical
65 trapping of oxygen in Atlantic Water and biological production (Kress and Herut, 2001; Di Biagio et al., 2022).
66 Beyond the seasonal signal associated with local processes, the properties of the upper layer are also influenced by
67 the general eastern Mediterranean circulation and in particular the Adriatic-Ionian Bimodal Oscillation System (BiOS)
68 (Gacic et al., 2010, 2011; Velaoras et al. 2014; Menna et al., 2022), characterized by two alternating circulation
69 regimes: during the anti-cyclonic phase of the Northern Ionian Gyre (NIG), Atlantic Water (AW) flowing across the
70 Sicily Channel is preferentially directed northwards, toward the Adriatic Sea, while during its cyclonic phase, AW,
71 directed eastward, mostly supplies the Levantine Basin. The BiOS process presents quasi-decadal variability and has
72 been proposed as a driver of changes in the thermohaline and biogeochemistry in the Adriatic and Levantine seas
73 (Civitarese et al., 2010; Velaoras et al. 2014; Ozer et al., 2017; Ozer et al., 2022; Di Biagio et al., 2023; Civitarese et

74 al., 2023). Below the euphotic layer, oxygen concentrations decline with an Oxygen Minimum Layer (OML) located
75 below the Intermediate Water between 600 and 1200 m (Cardin et al., 2015; Mavropoulou et al., 2020) and
76 characterized by concentrations of 170/180 $\mu\text{mol kg}^{-1}$ (Tanhua et al., 2013). Deep water masses of the sub-basin are
77 sensitive to variations in deep-water formation and circulation taking place in the Eastern Mediterranean. After the
78 Eastern Mediterranean Transient (EMT) in the early 1990's when the deep water formation area shifted from the
79 Adriatic to the Aegean Sea, an increase of oxygen was documented in the deeper layers in response to the inflow
80 below 2500 m of more oxygenated waters originating from the Aegean Sea (Lascaratos et al., 1999; Mavropoulou et
81 al., 2020). This was accompanied with the upward displacement of the older Adriatic-origin deep waters and of the
82 OML. More recent observations, however, indicate a deoxygenation trend since 2008, attributed to weakened deep
83 water formation and reduced ventilation rates as a progressive return to pre-EMT characteristics with an homogenized
84 deep layer (Sisma-Ventura et al., 2021).

85 To date, with limited spatial and temporal observations in the area, the variability of oxygen inventory in the Levantine
86 Basin remains poorly understood, and there is no proposed comprehensive budget quantification for the entire region.
87 In the framework of the PERLE (Pelagic Ecosystem Response to Deep Water Formation in the Levant Experiment,
88 Conan and Durrieu De Madron, 2019) project, the present work aims at quantifying the seasonal and interannual
89 variations in the oxygen inventory of the Levantine surface and intermediate water masses, detailing the contribution
90 of air-sea oxygen fluxes, biogeochemical and physical fluxes. This analysis is based on 3D coupled hydrodynamic-
91 biogeochemical model outputs covering a period of 7 years, from 2013 to 2020. Following on the budget approach
92 developed by Ulses et al. (2021) for the north-western Mediterranean Sea, we investigate the ultra-oligotrophic
93 Levantine Basin and provide a basin-scale quantification of its dissolved oxygen budget, highlighting the role of
94 transport processes and permanent circulation features such as the Rhodes Gyre.

95 After the introduction (Sect. 1), this paper is organized as follows. Sect. 2 describes the coupled hydrodynamic-
96 biogeochemical model implemented in the Levantine Basin and an assessment of the model results using *in situ*
97 observations. Sect. 3 investigates the seasonal and interannual dynamics of oxygen in the surface and intermediate
98 layers for the Levantine Basin, estimates an annual budget of oxygen, and finally describes its spatial variability. This
99 section is followed by a discussion of the results and a conclusion in Sect. 4 and 5, respectively.



100

101 **Figure 1: Model domain and bathymetry (m, background) in the Eastern Mediterranean. The arrows represent**
 102 **the simulated surface currents averaged over the study 7-year period (2013-2020), black thick lines delimit**
 103 **the basin for the budget calculation. Red, yellow, and green dots indicate BGC-Argo floats trajectories, PERLE-1,**
 104 **and PERLE-2 cruise stations, respectively, and white crosses CARIMED cruise stations, over the period from**
 105 **2013 to 2021. Blue dots in the insert represent the river mouths.**

106

107 **2. Material and Method**

108 **2.1 Modeling**

109 **2.1.1 The coupled hydrodynamic-biogeochemical model**

110 This study is based on a Mediterranean configuration of the ocean circulation model SYMPHONIE (Marsaleix et al.
 111 2006; 2008), forcing offline the biogeochemical model Eco3M-S (Ulses et al., 2016; 2023). The horizontal resolution
 112 of the model grid varies from 2.3 to 4.5 km, with a refined resolution of 1.3 km in the Gibraltar Strait. The vertical
 113 grid has 60 vertical vanishing quasi sigma levels. More details can be found in Estournel et al. (2021).

114 Eco3M-S is a multi-nutrient and multi-plankton functional type model, representing the dynamics of the pelagic
 115 plankton ecosystem and the cycles of carbon, nitrogen, phosphorus, silicon, and oxygen (Auger et al., 2011; Ulses et
 116 al., 2023), with 37 state variables. The rate of change of dissolved oxygen concentration due to biogeochemistry in
 117 the water column is calculated based on the following equation:

$$\begin{aligned}
118 \quad \frac{dDOx}{dt} &= \sum_{i=1}^3 (GPP_i - RespPhy_i) \gamma_{C/DOx} - \sum_{i=1}^3 (RespZoo_i) \gamma_{C/DOx} - RespBac \gamma_{C/DOx} \\
119 \quad &+ (UptPhy_{i,NO_3} - Nitrif) \gamma_{NH_4/DOx} \quad (\text{Eq. 1})
\end{aligned}$$

120 The dissolved oxygen concentration is represented by the term DOx . GPP_i and $RespPhy_i$ are gross primary production
121 and respiration, respectively, for phytoplankton group i . $RespZoo_i$ and $RespBac$ are respiration of zooplankton group
122 i and of bacteria, $UptPhy_{i,NO_3}$, and $Nitrif$ uptake of nitrate by phytoplankton class i , and nitrification, respectively.
123 $\gamma_{C/DOx}$ and $\gamma_{NH_4/DOx}$, equal to 1 and 2, respectively, are the moles of DOx used per mole of C in respiration and
124 needed to oxidize one mole of ammonium in nitrification as described in Grégoire et al. (2008). The flux of dissolved
125 oxygen at the air-sea interface is calculated using the Garcia and Gordon (1992) equation for the solubility, and the
126 parametrization of Wanninkhof and McGillis (1999) for the transfer velocity, following the study of Ulses et al. (2021)
127 in the northwestern Mediterranean deep convection area.

128 2.1.2 Initialisation and boundary conditions

129 The implementation of the coupled model was described in detail in Estournel et al. (2021) and Habib et al. (2023).
130 The period simulated by the hydrodynamic model runs from May 2011 to May 2021. Atmospheric forcings for both
131 hydrodynamic and biogeochemical models were provided by the HRES (atmospheric model High RESolution
132 forecast) product of ECMWF model with a horizontal resolution of $1/8^\circ$ using hourly fields (wind, air temperature
133 and humidity, pressure, solar and downward longwave radiation, and precipitation). The biogeochemical model
134 Eco3M-S was forced by daily fields of temperature, salinity, current, and vertical diffusivity from the SYMPHONIE
135 model. It covers the period between August 2011 till March 2021. The first two years (July 2011–December 2013) of
136 the biogeochemical simulation were dedicated to model spin-up to ensure biogeochemical stability and were not
137 considered in the analysis, while the December 2013– December 2020 period was used for the budget analysis. This
138 period was selected based on the availability of consistent physical forcing and the density of in situ observations for
139 model initialization and validation. The biogeochemical model was initialized using climatological fields of in situ
140 nutrient and dissolved oxygen concentrations from the CARIMED (CARbon in the MEDiterranean Sea, Alvarez et
141 al., 2019) database and Biogeochemical-Argo (BGC-Argo) float data over the 2011-2012 summer periods when data
142 were available, in 10 sub-regions. At the mouths of 142 rivers taking into account (Fig. 1), concentrations of nutrients
143 were imposed by sub-basin using the dataset of Ludwig et al. (2010). Dissolved oxygen at river mouths was set at
144 saturation values. In the Atlantic Ocean, nutrients were prescribed using monthly profiles from the World Ocean Atlas
145 2009 climatology at $5.5^\circ W$. In the Marmara Sea, to represent a two-layer flow regime, we imposed a daily relaxation
146 towards a nutrient concentration of 0.24 and 1.03 $mmol N m^{-3}$ and a phosphate concentration of 0.06 and 0.05 $mmol$
147 $P m^{-3}$ for depths above and below 15 m, respectively, based on the observations near the Dardanelles Strait from
148 (Tugrul et al., 2002).

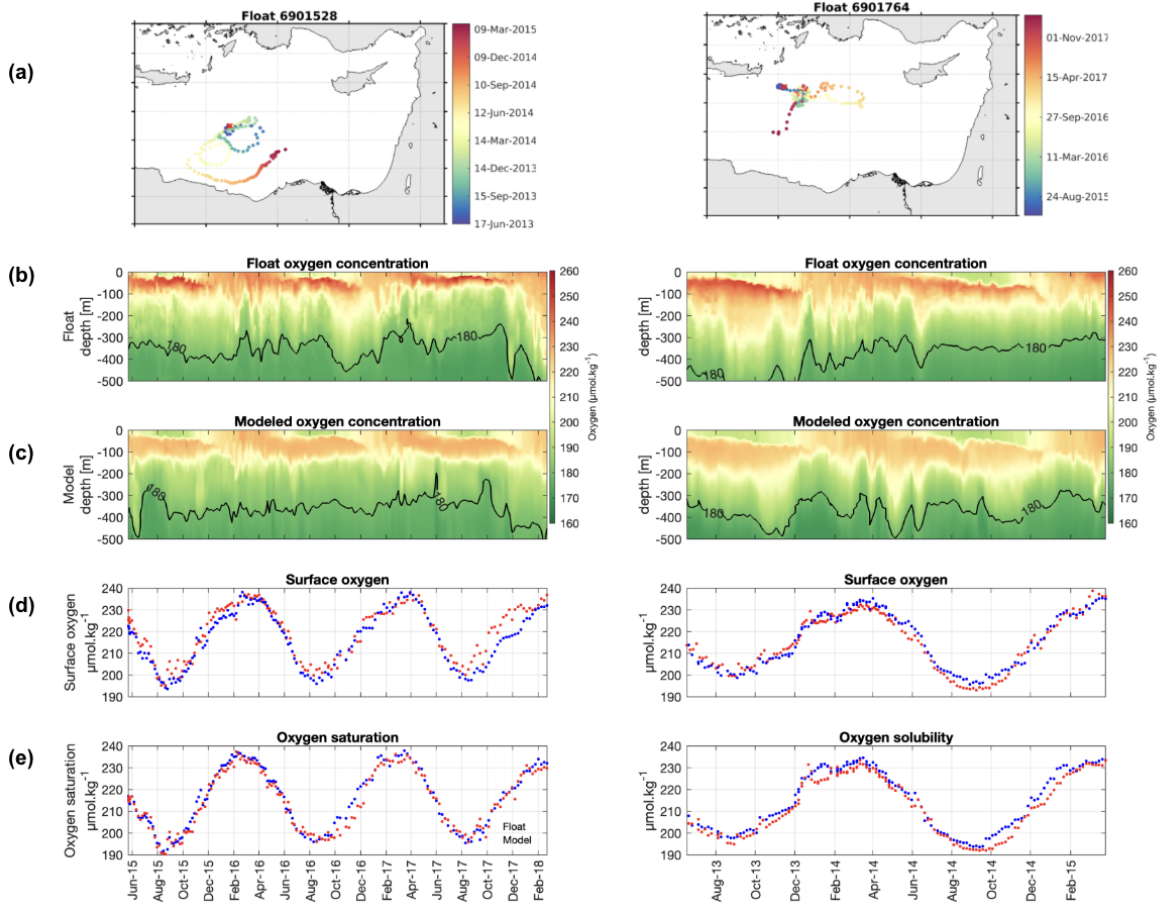
149 2.1.3 Budget calculation

150 For spatial mean and budget calculation, we defined an area (delimited by the black lines in Fig. 1) covering 540 000
151 m^2 , with the boundary with the Ionian Sea linking the southwestern Cretan coast to the Libyan coast. The water column
152 was divided into three layers based on the thermohaline structure represented by the physical model (Estournel et al.,

153 2021) and the associated dominant biogeochemical processes: the surface layer defined as the photic layer covering
154 the surface to 150 m depth where photosynthesis takes place, the underlying intermediate layer from 150 to 400 m
155 where LIW flows, and the deep layer below 400 m. In this study, we will be focusing on the first two layers where
156 changes, in particular related to LIW formation, occur generally more rapidly. The biogeochemical term of the oxygen
157 budget is the sum of oxygen production due to gross primary production and nitrate uptake by phytoplankton, and of
158 oxygen consumption through nitrification and community respiration. The physical term is divided into two
159 components: the lateral and the vertical transports, which are both due to advection and mixing processes. The lateral
160 transport represents the exchanges at the boundaries with the Ionian and Aegean seas. A negative lateral transport
161 indicates a net export of oxygen from the considered layer of the Levantine Basin. The oxygen inventory, air-sea
162 fluxes, biogeochemical fluxes, and lateral fluxes were calculated online while the vertical transport, defined as a net
163 flux at the layer interface, was deduced from the other terms of the budget. The budget calculation is detailed in Text
164 S1 in Supplement Material.

165 **2.2 Model assessment**

166 An assessment of the hydrodynamic and biogeochemical simulations in the surface and intermediate water masses has
167 been performed in previous studies (Estournel et al., 2021; Habib et al., 2023), suggesting its capacity to reproduce
168 the observed general hydrology and biogeochemistry (chlorophyll, dissolved inorganic nutrients, and dissolved
169 oxygen) in the Levantine Sea. Here, the model is further assessed in terms of the dissolved oxygen dynamics by
170 providing supplementary comparisons with observations from BGC-Argo floats (6901528 and 6901764,
171 <http://www.coriolis.eu.org>, Last access: 11 February 2026), PERLE cruises (PERLE-1 and PERLE-2,
172 <https://campagnes.flotteoceanographique.fr/campagnes/18000848/fr/>, Last access: 5 June 2025, Conan and Durrieu
173 De Madron, 2019), and those gathered in the CARIMED database (Alvarez et al., 2025), as well as from situ
174 measurements of metabolic rates.



175

176 **Figure 2: From top to bottom: (a) trajectory of the BGC-Argo floats with deployment position (red cross) and**
 177 **chronology in color; Hovmöller diagrams of oxygen concentration ($\mu\text{mol O}_2 \text{ kg}^{-1}$) from (b) float data and (c)**
 178 **model outputs for the first 500 m; (d) surface oxygen concentration in the first 10 m ($\mu\text{mol O}_2 \text{ kg}^{-1}$) and (e)**
 179 **oxygen solubility ($\mu\text{mol O}_2 \text{ kg}^{-1}$), from the float data (red) and the model (blue).**

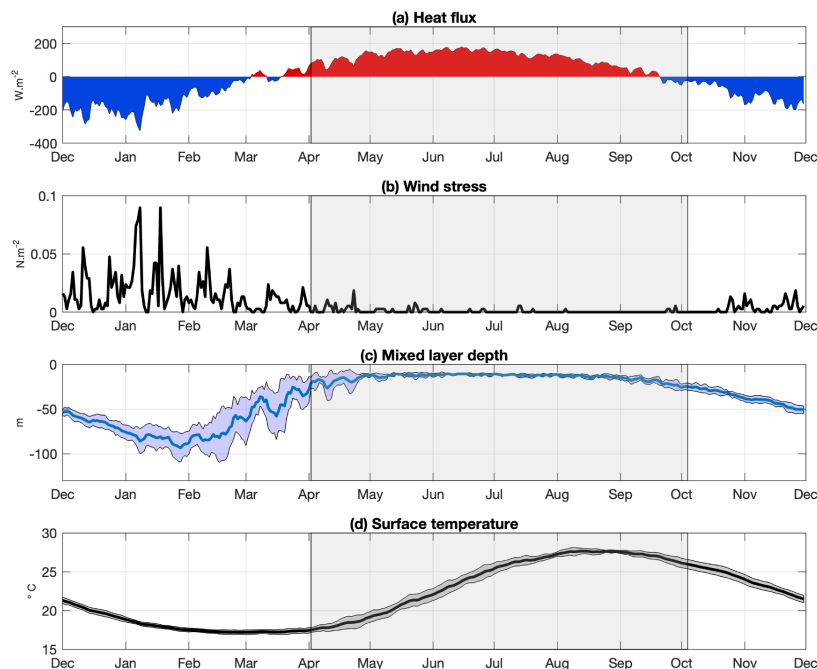
180 The model reproduces the observed seasonal and vertical variability (Fig. 2, Fig. S1), with strong agreement with
 181 observations throughout the upper 500 m, in particular in the timing and depth of the subsurface oxygen maximum
 182 and the oxygen minimum layer. The discrepancies found concern a slight underestimation of the subsurface oxygen
 183 maximum ($\text{RMSD} \approx 8 \mu\text{mol kg}^{-1}$) compared to the BGC-Argo float, and an overestimation below 100 m compared
 184 to PERLE-2 observations, likely due to an overestimation of remineralization processes or vertical diffusion. The
 185 model and in situ data significantly correlate with correlation coefficient higher than 0.95 ($p\text{-value} < 0.05$). The RMSD
 186 values (Root Mean Square Difference) between modeled and observed surface oxygen and solubility are less than 5
 187 $\mu\text{mol O}_2 \text{ kg}^{-1}$ for both Argo floats and fall within the oxygen uncertainty interval associated with Argo float data (~ 2 -
 188 $10 \mu\text{mol kg}^{-1}$ depending on the sensor, Grégoire et al., 2021). Finally, comparisons between model results with
 189 metabolic rate measurements near the surface and within the upper layer over the May-July period (BOUM cruise
 190 (Christaki et al. 2011); THRESHOLD cruises (Regaudie-de-Gioux et al., 2009); MINOS cruise (Moutin and
 191 Raimbault, 1996) indicate that modeled GPP (gross primary production), CR (community respiration) and NCP (net
 192 community production, corresponding to GPP minus CR) fall in the observed range, generally in their upper values

193 (Table S1). These comparisons show the model’s ability to represent oxygen-related biogeochemical processes in the
194 Levantine Basin.

195 3 Results

196 3.1 Seasonal variability

197 Figure 3 presents the mean annual cycle of the modeled air-sea heat flux, wind stress, mixed layer (ML) depth, and
198 surface temperature, spatially averaged over the Levantine Sea from December 2013 to December 2020. During fall,
199 the decrease in air temperature leads to significant sea surface heat loss, while intensified northern winds weaken
200 stratification, gradually deepening the mixed layer (Fig. 3a-c). The sea surface temperature drops significantly (Fig.
201 3d). Heat loss events persist through winter, leading the surface temperature to reach a minimum of approximately
202 17°C and the mixed layer depth to gradually increase, peaking in January/February. The yearly maximum ML depth
203 averaged spatially over the seven years is 108 ± 11 m (Table S2). In March/April, the sea surface starts gaining heat,
204 and the surface temperature increases (Fig. 3a and 3d). The ML abruptly shallows but still exhibits large variations
205 during early spring, in response to the events of continental cold winds. The frequency of intense wind events
206 decreases in late spring/summer (Fig. 3b). Surface temperature reaches maximum values around 28 °C in August (Fig.
207 3d), and a thin ML settles until October. In the following, the annual cycle is divided into two successive periods
208 based on the vertical mixing intensity. The first period is a mixing period, from October to March, and the second
209 period is a stratified period, from April to September. The two periods were defined based on a mixed layer depth
210 threshold of 25 m, following the criteria used by D’Ortenzio et al. (2008) and Houpert et al. (2015).



211

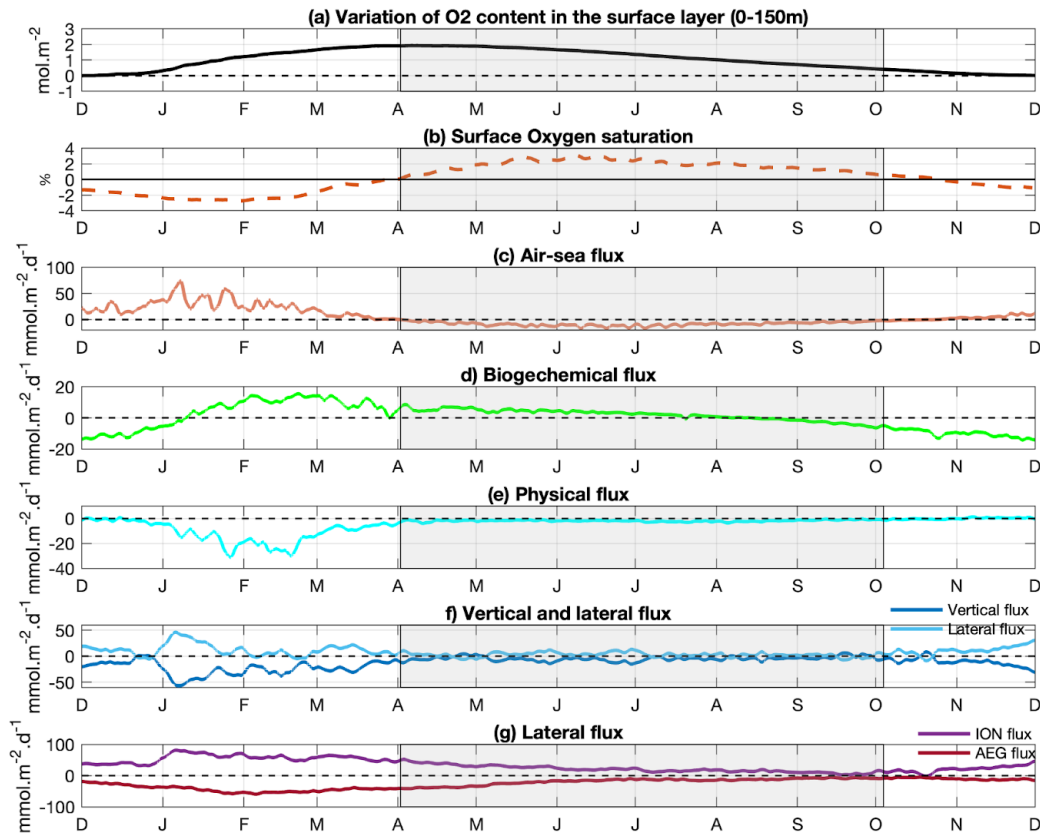
212 **Figure 3: Annual time series of modeled (a) air-sea heat fluxes ($W m^{-2}$), (b) wind stress ($N m^{-2}$), (c) mixed layer**
213 **depth (m), and (d) surface temperature ($^{\circ}C$), averaged over the Levantine Sea and the period 2013-2020. In (c)**

214 **and (d), the solid line corresponds to the temporal mean, the shaded area to the standard deviation. The grey**
215 **shaded area represents the stratification period.**

216 The annual cycle of the 7-year averaged oxygen fluxes and inventory variations is shown in Fig. 4 and 5 for the surface
217 and intermediate layers, respectively. In both layers, the oxygen content increases during the mixing period and
218 gradually decreases during the stratified period, with minimum values in November/December for the surface layer
219 and January for the intermediate layer (Fig. 4a and 5a). Both vertical and net horizontal transports exhibit a clear
220 seasonal variation, reaching maximum values of $50 \text{ mmol m}^{-2} \text{ day}^{-1}$ in the surface layer and $50 \text{ mmol m}^{-2} \text{ day}^{-1}$ and 40
221 $\text{mmol m}^{-2} \text{ day}^{-1}$, respectively in the intermediate layer (Fig. 4f and 5e). During the mixing period, and particularly
222 during events of strong winds and vertical mixing (Fig. 3b-c), oxygen is exported from the surface layer towards the
223 intermediate layer (Fig. 4f), and subsequently, from the intermediate towards the deep layer (Fig. 5e). The associated
224 mean export rates amount to 0.56 and $0.46 \text{ mol O}_2 \text{ m}^{-2} \text{ month}^{-1}$, respectively (Fig. S3b,d). During the stratified period,
225 the downward export of O_2 towards the intermediate and deeper layers is reduced by 75% and 40%, respectively (Fig.
226 S3d).

227 Horizontal oxygen transport in the surface layer is characterized by a net inflow from the Ionian Sea and an outflow
228 towards the Aegean Sea (Fig. 4g, S2b). These exchanges are stronger during the mixing period than during the
229 stratified period (with inflow of 1.3 versus $0.6 \text{ mol O}_2 \text{ m}^{-2} \text{ month}^{-1}$ from the Ionian Sea and outflow of 0.9 versus 0.5
230 $\text{mol O}_2 \text{ m}^{-2} \text{ month}^{-1}$ from the Aegean Sea, respectively, Fig. S3b). In the intermediate layer, horizontal exchanges are
231 weaker overall but still display a seasonal signal. During the mixing period, a stronger net inflow from the Ionian Sea
232 ($0.2 \text{ mol O}_2 \text{ m}^{-2} \text{ month}^{-1}$) and a stronger outflow towards the Aegean Sea ($-0.4 \text{ mol O}_2 \text{ m}^{-2} \text{ month}^{-1}$, Fig. S3d and 5f)
233 are obtained. While the net oxygen transport in the surface layer remains directed from the Ionian and towards the
234 Aegean across both periods, the intermediate layer exhibits net oxygen export toward both the Aegean and Ionian
235 Seas during the stratified period, accounting for 96% and 4% of the total horizontal export respectively (Fig. S3d).

236 Model results indicate that the ecosystem in the surface layer of Levantine Basin acts as a net source of dissolved
237 oxygen from January to August, with the highest production between February and March. In contrast, net
238 consumption dominates from September to December (Fig. 4d). Overall, the biogeochemical O_2 flux results in a mean
239 oxygen loss of $0.03 \text{ mol m}^{-2} \text{ month}^{-1}$ during the mixing period (from October to April) and a gain of 0.06 mol m^{-2}
240 month^{-1} during the stratified period (Fig. S3a). Maximum magnitudes of biological production ($> 2 \text{ mmol O}_2 \text{ m}^{-2} \text{ day}^{-1}$)
241 are located near the surface during the periods of winter mixing and the associated phytoplankton bloom, before
242 shifting to subsurface layers later in the year (Fig. S4f). Oxygen consumption peaks in fall between 100 and 200 m
243 depth, and during the mixing period below the mixed layer. During the stratified period, a relatively thick subsurface
244 oxygen maximum (SOM) layer persists around 70 m depth, overlying the subsurface maximum of biological
245 production located at around 140 m depth, close to the deep chlorophyll maximum (Fig. S4b, c, and f). This is in
246 agreement with the findings of the modelling study of Di Biagio et al. (2022). In the intermediate layer (150-400 m),
247 the ecosystem is characterized by a loss of oxygen throughout the year, with biogeochemical fluxes reaching values
248 lower $-5 \text{ mmol m}^{-2} \text{ day}^{-1}$ (Fig. 5b).



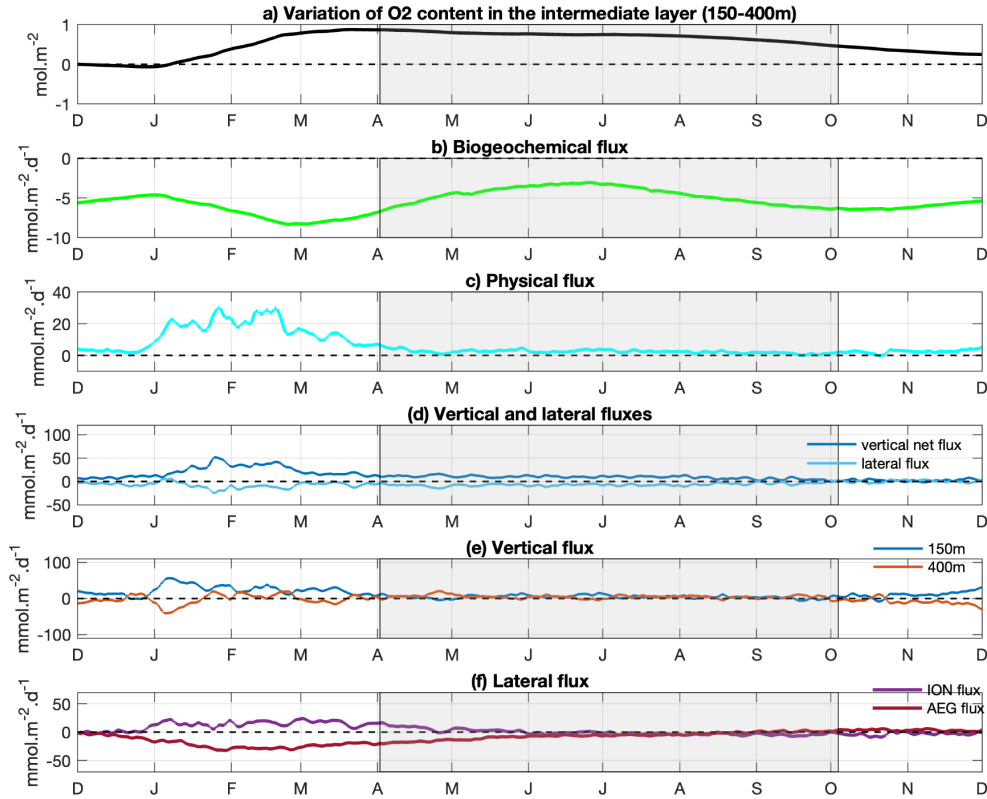
249

250 **Figure 4: Oxygen concentration and budget of the 0-150 m layer of the Levantine Basin averaged over the**
 251 **period of study. (a) Variation of the dissolved oxygen inventory (mol m^{-2}) relative to initial conditions (Values**
 252 **are normalized to the starting time point), (b) surface oxygen saturation (orange) = $(\text{DOx} - \text{DOx sat})/\text{DOx sat}$**
 253 **$\times 100\%$), (c) air-sea flux (positive values correspond to downward fluxes, $\text{mmol O}_2 \text{ m}^{-2} \text{ day}^{-1}$), (d) biogeochemical**
 254 **flux ($\text{mmol O}_2 \text{ m}^{-2} \text{ day}^{-1}$), (e) sum of vertical (through the 150 m depth) and lateral (exchanges with the Ionian**
 255 **and Aegean Seas) transport fluxes ($\text{mmol O}_2 \text{ m}^{-2} \text{ day}^{-1}$), (f) vertical (light blue) and lateral (dark blue) fluxes**
 256 **($\text{mmol O}_2 \text{ m}^{-2} \text{ day}^{-1}$), (g) lateral fluxes at the boundary with the Ionian (purple) and Aegean (red) Seas (mmol**
 257 **$\text{O}_2 \text{ m}^{-2} \text{ day}^{-1}$). Horizontal transport fluxes are scaled to the area of the Levantine Basin for comparison with the**
 258 **other budget terms. The grey shaded area represents the stratification period.**

259 The air-sea oxygen flux displays a marked seasonal pattern (Fig. 4b). During the October-April mixing period, the
 260 Levantine Basin, which is undersaturated in oxygen compared to the atmosphere, acts as a sink of atmospheric oxygen.
 261 From September onward, oxygen solubility has increased (Fig. 4b) with the decrease in surface temperature (Fig. 3d)
 262 since September. In parallel, the gradual deepening of the mixed layer favors an increase in the surface oxygen
 263 concentration, through the mixing of surface O_2 poorer waters with subsurface O_2 -rich waters (Fig. S4c), although
 264 surface concentrations remain below the saturation level. The air-sea flux is particularly strong in winter under strong
 265 wind conditions, and reaches maximal values around $70 \text{ mmol m}^{-2} \text{ day}^{-1}$ in early January (Fig. 4c). When averaged
 266 over the mixing period, the air-sea flux amounts to $0.50 \text{ mol O}_2 \text{ m}^{-2} \text{ month}^{-1}$ (Fig. S3a). At the onset of the stratified
 267 period (April - May), surface oxygen concentration increases to $230 \mu\text{mol kg}^{-1}$, slightly exceeding saturation levels
 268 due to biological oxygen production in the surface layer (Sect. 3.2.4). As a result, the Levantine Basin becomes a

269 source of oxygen for the atmosphere (Fig. 4c). During the rest of the stratified period, the surface oxygen concentration
 270 continues to present values higher than the oxygen solubility, leading to continuous outgassing of O₂. We estimate a
 271 mean net release of 0.26 mol O₂ m⁻² month⁻¹ of oxygen to the atmosphere over the whole stratified period (Fig. S3a).

272



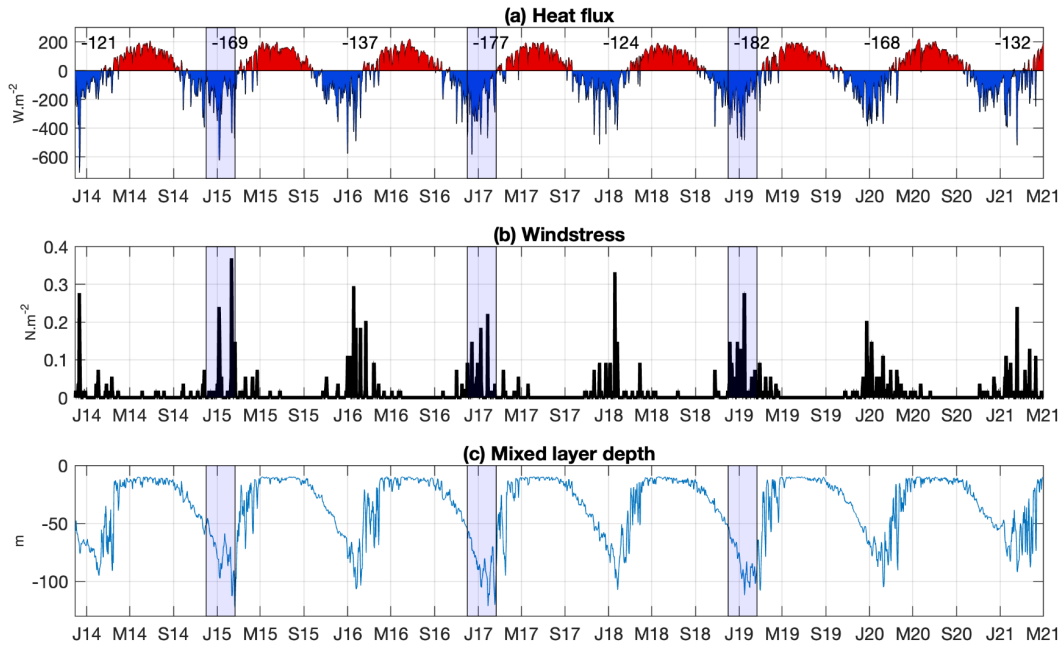
273

274 **Figure 5: Mean annual cycle of (a) variation of the dissolved oxygen inventory (mol m⁻²) relative to initial**
 275 **conditions (Values are normalized to the starting time point), and the different oxygen fluxes (mmol m⁻² day⁻¹):**
 276 **(b) biogeochemical flux, (c) total vertical and horizontal transport, (d) vertical (downward) flux (light blue) and**
 277 **lateral flux (dark blue), (e) the vertical fluxes at 150 and 400m and (f) the lateral Ionian (purple) and Aegean**
 278 **(red) fluxes, in the intermediate layer (150-400 m) and averaged over the Levantine Basin. The grey shaded**
 279 **area represents the stratification period.**

280 3.2. Interannual variability

281 The analysis of the seasonal cycle shows that oxygen fluxes exhibit their largest variability during winter, as reflected
 282 by higher standard deviations. In addition, correlations between annual oxygen processes (NCP, downward export,
 283 ...) and seasonal fluxes indicate that winter is the most influential season on oxygen dynamics (Fig. S5). Therefore,
 284 the following section focuses on winter conditions to investigate the interannual variability of oxygen-related
 285 processes. Winter (December-January-February) heat loss exceeds the seasonal mean value of 152 W m⁻² for years
 286 2014-15, 2016-17, 2018-19, and 2019-20 (Fig. 6a, Table S2). In contrast, wind stress does not show consistent
 287 interannual signals, with peak values around 0.2 N m⁻² occurring every winter (Fig. 6b). The ML depth presents

288 interannual variability primarily associated with variations in heat loss fluxes (Fig. 6a and 6c). ML deeper than the 7-
 289 year mean value of 108 m are found during the winters 2014-15, 2016-17, and 2018-19 (Table S2). Based on the mean
 290 winter heat flux (W-HF), and mean and maximum ML, the years were classified into two categories: as mild and cold
 291 winter years. Years with both winter heat loss and maximum ML above the seven-year means, i.e. 2014-15, 2016-17
 292 and 2018-19, are classified as cold winter years, whereas the remaining years, 2013-14, 2015-16, 2017-18 and 2020-
 293 21, are classified as mild years.



294

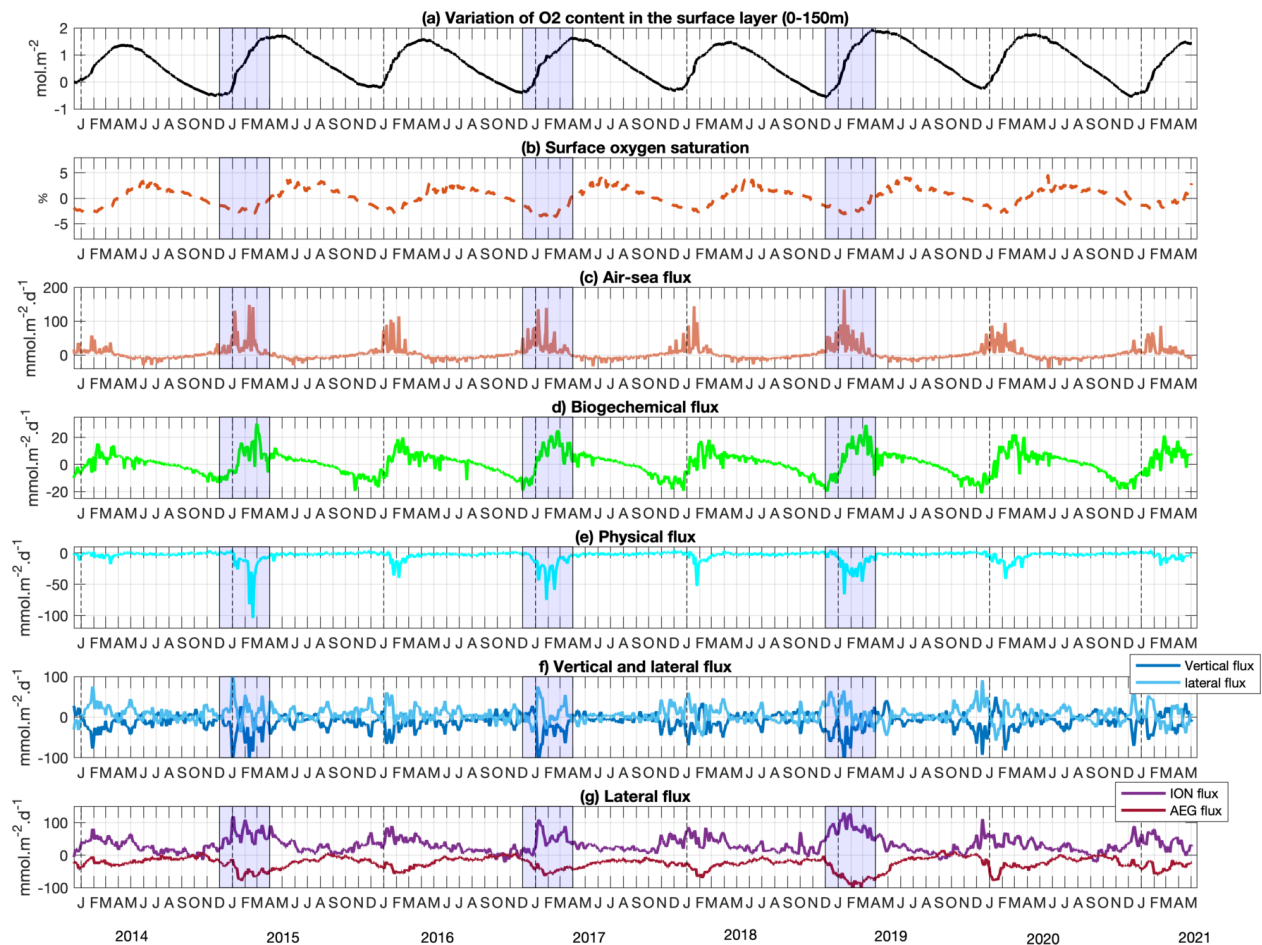
295 **Figure 6: Time series of modeled (a) air-sea heat fluxes ($W m^{-2}$), (b) wind stress ($N m^{-2}$), and (c) mixed layer**
 296 **depth (m), averaged over the Levantine Basin. The mean winter (December-January-February) heat loss is**
 297 **indicated in (a). The blue shaded area represents the winter of the cold winter years.**

298 All years display qualitatively similar seasonal oxygen cycles in the surface layer (Fig. 7). However, cold winter years
 299 (2014–15, 2016–17, 2018–19) exhibit substantially larger oxygen fluxes and stronger inventory variations. During
 300 these winters, changes in oxygen inventory exceed $2 \text{ mol O}_2 \text{ m}^{-2}$ (Fig. 7a). During phytoplankton blooms in these cold
 301 winters, biogeochemical fluxes surpass $20 \text{ mmol m}^{-2} \text{ day}^{-1}$ (Fig. 7d). Lateral and vertical transports of dissolved oxygen
 302 at the surface layer boundaries are also enhanced during cold winters. Lateral inflow from the Ionian Sea, lateral
 303 outflow toward the Aegean Sea, and downward export to the intermediate layer, show peak values exceeding 100, 75,
 304 and $100 \text{ mmol m}^{-2} \text{ day}^{-1}$, respectively (Fig. 7f–g). In addition, air-sea oxygen fluxes also exceed $150 \text{ mmol m}^{-2} \text{ day}^{-1}$
 305 during cold winters (Fig. 7c).

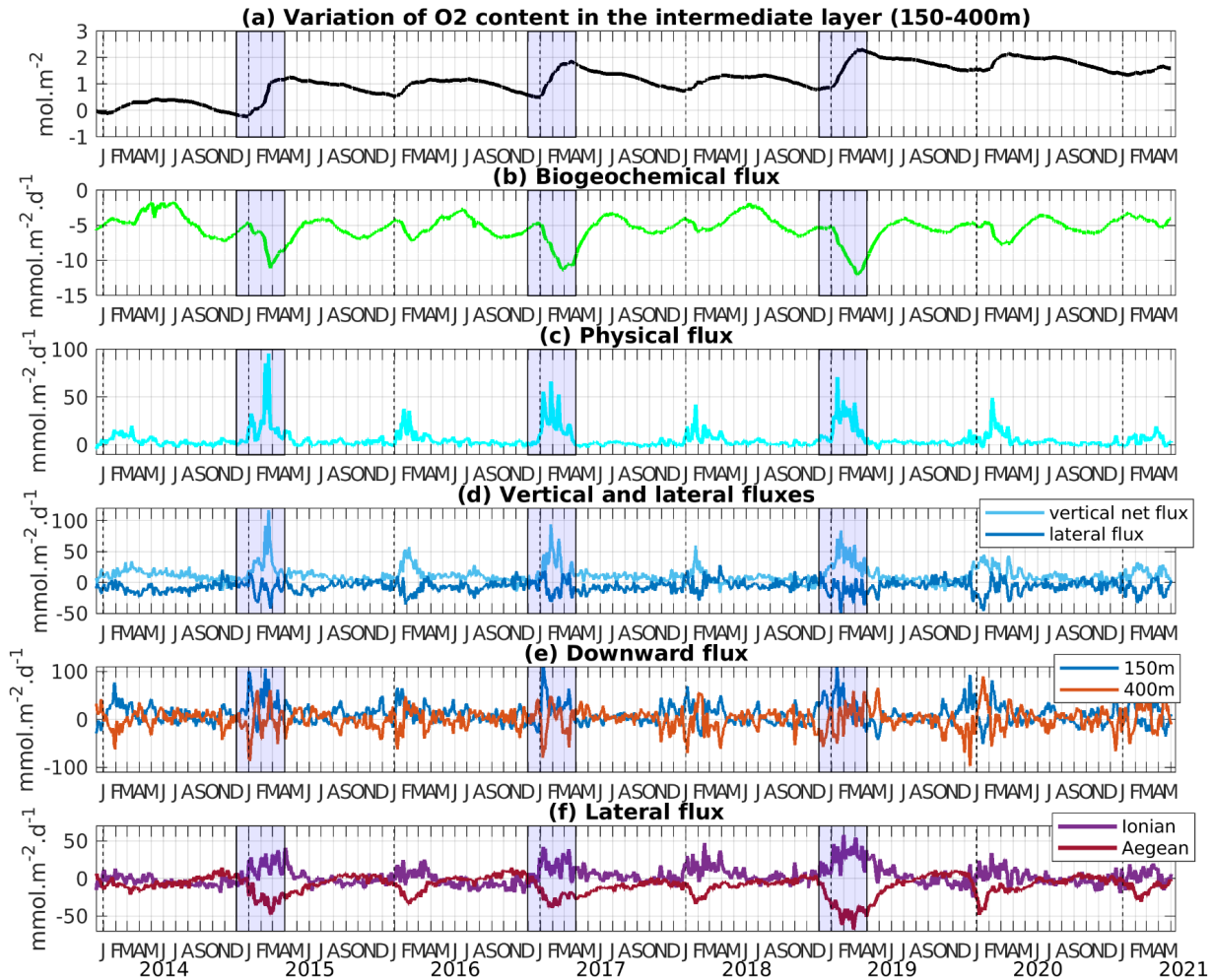
306 In the intermediate layer, cold winter years likewise display the strongest O_2 winter fluxes and the largest oxygen
 307 inventory variation compared to mild winter years (Fig. 8). Biogeochemical fluxes exhibit pronounced negative peaks
 308 exceeding $-10 \text{ mmol m}^{-2} \text{ day}^{-1}$ during cold winter years (Fig. 8b). While these negative extrema are not significantly
 309 stronger than those obtained in mild years, the subsequent positive fluxes following cold winters are markedly
 310 enhanced, except during 2016-17. Physical fluxes also are marked by larger magnitudes during cold winters (Fig. 8c-
 311 f), with enhanced lateral and vertical oxygen exchanges, as found in the upper layer. Along with the seasonal internal

312 variation, an increasing trend in the inventory is visible from 2013-14 to 2018-19, followed by a decreasing trend until
 313 the end of the study period (Fig. 8a).

314 Overall, oxygen flux variability is partly linked to the variability of winter heat loss (W-HL). A strong correlation is
 315 found between mean W-HL and winter downward oxygen export from the surface layer ($R = 0.76$, p -value < 0.05 ,
 316 Fig. S5). Cold years also show enhanced NCP (Net Community Production: gross primary production (GPP) minus
 317 community respiration (CR)), with a significant correlation between mean W-HL and annual NCP ($R = 0.91$, p -value
 318 < 0.05 , Fig. S5). When W-HL drops below 135 W m^{-2} , the trend suggests a shift of the system from autotrophic to
 319 heterotrophic conditions. In the intermediate layer, annual oxygen consumption remains relatively stable but is still
 320 significantly correlated with W-HL ($R = 0.94$, p -value < 0.05). Air-sea oxygen fluxes also show strong correlations
 321 with W-HL, both at the annual scale ($R = 0.92$, p -value < 0.05) and during winter ($R = 0.93$, p -value < 0.05). Although
 322 lateral fluxes intensify during cold years, only exchanges with the Aegean Sea show a significant correlation with W-
 323 HL ($R = 0.74$ in the surface layer, $R = 0.82$ in the intermediate layer). Correlations with exchanges from the Ionian
 324 Sea are weaker and not statistically significant ($R = 0.69$, p -value < 0.08).



325
 326 **Figure 7: As in Figure 4, but showing the interannual variability of oxygen inventory and budget components**
 327 **for the 0–150 m layer of the Levantine Basin. Blue shading marks cold winters.**



328

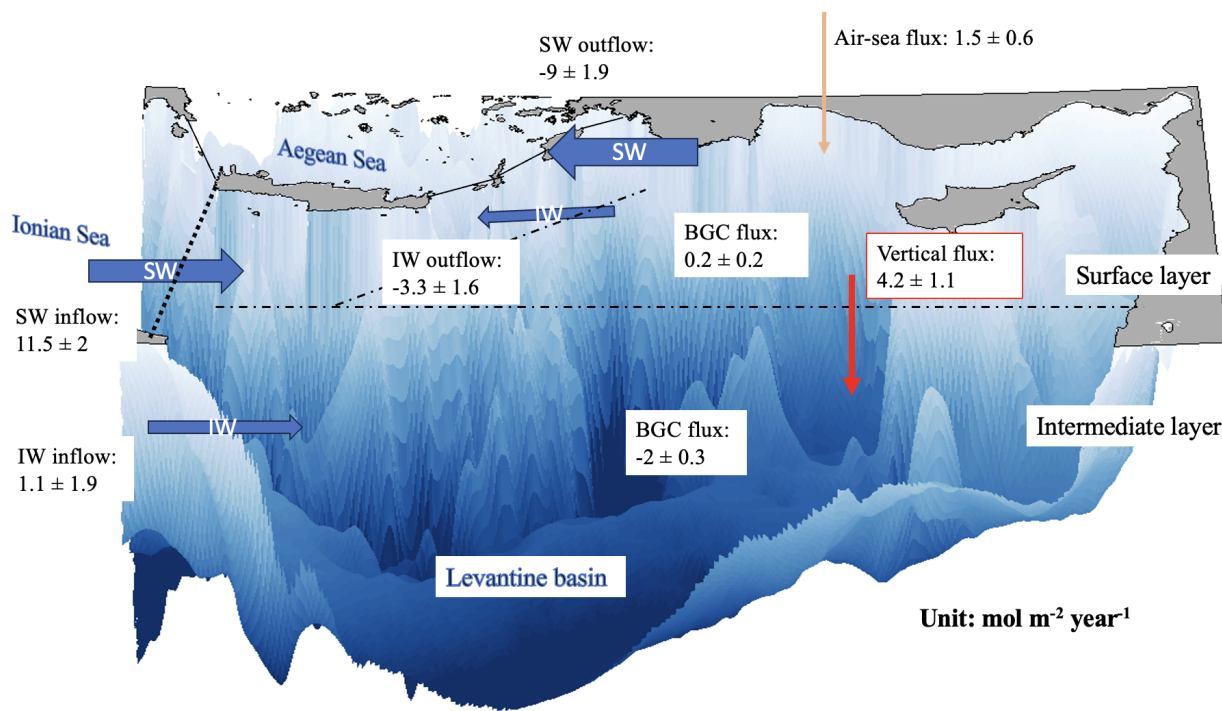
329 **Figure 8:** As in Figure 5, but showing the interannual variability of oxygen inventory and budget
 330 components for the 150-400 m layer of the Levantine Basin. The blue shaded area represents the winter of the
 331 cold winter years.

332 **3.3 Annual oxygen budget in the surface and intermediate layers**

333 On an annual basis and averaged over the seven studied years (Fig. 9), the surface ecosystem of the Levantine Basin
 334 generally acts as a net source of oxygen, although the magnitude and even the sign of the biogeochemical contribution
 335 vary substantially from year to year. The surface layer of the basin also exhibits a net gain of oxygen through air-sea
 336 exchange. This atmospheric input results from the seasonal alternation between wintertime uptake and summertime
 337 outgassing described in Sect. 3.1. In addition to the important air-sea fluxes, the basin receives a significant lateral
 338 supply of oxygen through the advection of waters originating from the Ionian Sea into the surface layer. A fraction of
 339 the oxygen supplied to the surface is exported downward toward intermediate depths, partially consumed by
 340 biogeochemical processes, while a remaining fraction is transported toward the Aegean Sea. On average, the oxygen
 341 budget indicates that the net biogeochemical oxygen flux is one order of magnitude smaller than the contributions
 342 from transport and air-sea exchange.

343 In the intermediate layer, the oxygen loss due to biogeochemical consumption is compensated by transport, at the
 344 annual scale (Fig. 9). The physical supply to the intermediate layer arises from both downward transport from the
 345 surface layer and lateral inflow from the Ionian Sea. A fraction of oxygen in intermediate waters is also exported
 346 toward the Aegean Sea (Fig. 9).

347 One can notice that in the surface layer, the lateral export of oxygen towards the Aegean Sea is smaller than the net
 348 input from the Ionian Sea, and on the contrary, in the intermediate layer, the lateral oxygen export toward the Aegean
 349 Sea is larger than the input from the Ionian Sea. This reflects both a small biological production in the surface layer
 350 and a large supply of oxygen from the surface layer into the intermediate waters through vertical transfer, occurring
 351 mostly during winter mixing, convection and subduction in the Levantine Sea. This budget highlights the role of the
 352 Levantine Basin as both a regional sink for intermediate waters and a transit zone for dissolved oxygen within the
 353 eastern Mediterranean circulation.



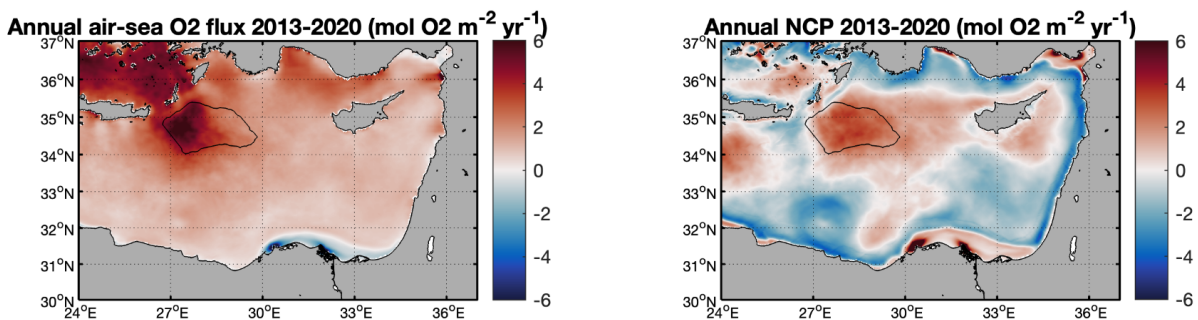
354
 355 **Figure 9: Schematic showing the terms of the mean annual oxygen budget (in mol O₂ m⁻² yr⁻¹) for the Levantine**
 356 **Basin over the period from December 2013 to December 2020. The terms of the budget are estimated for the**
 357 **upper (surface-150 m) and intermediate (150-400 m) layers. SW: surface layer, IW: intermediate layer.**

358 3.4 Spatial variability of oxygen fluxes in the Levantine Basin

359 At the annual scale, the whole Levantine Basin appears as an atmospheric sink for oxygen, except in the coastal area
 360 influenced by the Nile River (Fig. 10a). In the offshore region, the strongest oxygen uptake rates are found in the
 361 Rhodes Gyre area, covering 5% of the surface of the Levantine Basin, but contributing 14% of the annual atmospheric
 362 oxygen intake. Additional regions of enhanced uptake rates are located in the North, in the Antalya Bay and the

363 Cilician Basin identified as another LIW formation area (Fach et al. 2021). The spatial distribution of the annual air-
 364 sea oxygen flux is largely controlled by the winter air-sea O₂ flux (not shown). The annual anomalies show that cold
 365 years (2014-15, 2016-17 and 2018-19) are associated with enhanced atmospheric oxygen uptake over the entire basin
 366 (Table S3), and especially in the Rhodes Gyre (Fig. S8). In this main area of intermediate water formation, the vertical
 367 mixing period is characterized by the upward supply of colder and oxygen-poorer water from intermediate depths to
 368 the surface, more pronounced than in surrounding areas. The resulting negative temperature and oxygen anomaly
 369 reinforce surface undersaturation in this area, reaching maximum values varying between 2 and 5 % (with higher
 370 values during cold winter years). In contrast to the basin-wide functioning, where oxygen is generally exported
 371 downward from surface to intermediate layers, the Rhodes Gyre displays an inverse pattern. In this area, oxygen is
 372 transported upward from intermediate depths toward the surface, and subsequently redistributed laterally. This lateral
 373 transfer is particularly strong during winter and is associated with the dispersal of LIW by subduction (Estournel et
 374 al., 2021).

375 Model results also show a marked spatial heterogeneity in the balance between GPP and CR, expressed through net
 376 community production (NCP), when averaged over the period of study in the surface layer (surface-150 m; Fig. 10b).
 377 Positive NCP values are found in a central region encompassing the cyclonic Rhodes Gyre and other cyclonic gyres
 378 (e.g., West Cyprus gyres), as well as in the coastal areas influenced by river inputs. In particular, the Rhodes Gyre
 379 contributes to 41% of the total annual biological oxygen production in the surface layer of the entire basin. In contrast,
 380 negative values of NCP prevail in the along-slope circulation, and within the anticyclonic Mersa-Matruh Eddies and
 381 Shikmona Eddy. Annual NCP follows the same spatial pattern throughout all the years with a more pronounced
 382 production in the cyclonic gyres during cold years compared to mild winters (Fig. S7).



383
 384 **Figure 10: Modeled annual air-sea oxygen flux and net community production (NCP, mol O₂ m⁻² yr⁻¹) in the**
 385 **surface layer (0-150 m) for the period from December 2013 to December 2020. The black line delimits the**
 386 **Rhodes Gyre. Positive values for the air-sea oxygen flux indicate a net flux of oxygen into the ocean (uptake),**
 387 **while negative values indicate a net flux from the ocean to the atmosphere. Positive NCP values correspond to**
 388 **net biological oxygen production and negative values to consumption.”**

389 4 Discussion

390 In the present study, we used a 3D coupled physical-biogeochemical model to investigate the dynamics of oxygen in
 391 the Levantine Basin. The physical and biogeochemical parts of the coupled model were previously validated by
 392 Estournel et al. (2021) and Habib et al. (2023), respectively. Here we have further compared our results on the oxygen

393 cycle with two types of in situ observations: high-resolution BGC-Argo data and data from research cruises. The major
394 limitation highlighted by these comparisons is the representation of the subsurface oxygen maximum layer. The
395 marked heterogeneity of this layer in observations, with maximum concentrations in its upper part followed by a
396 progressive decrease of its value with depth, is not fully reproduced in the model. The increase of the maximum value
397 during the summer period, shown in the BGC-Argo data, may reflect production or respiration processes that are
398 underestimated or overestimated, respectively, in the model. Alternatively, this discrepancy may be explained by
399 physical processes with a misrepresentation of the thickness of the subsurface oxygen maximum layer in the model.
400 In that case, a finer vertical resolution at those depths or an improvement of the vertical advection scheme, avoiding
401 possible spurious numerical mixing, as proposed by Garinet et al. (2024), could be tested in future works to reduce
402 potential excessive vertical diffusivity.

403 Our budget of oxygen is subject to sources of uncertainties linked to the physical and biogeochemical models used in
404 this study. One approach to overcome single-model uncertainties and limitations would be to adopt a multi-model
405 approach. An alternative approach would consist in estimating oxygen budgets using observational syntheses;
406 however, the sparse spatial coverage of in situ data currently limits the closure of basin-scale oxygen budgets based
407 solely on observations. Finally, a complementary strategy could involve a combined approach such as that developed
408 by Di Biagio et al. (2023) which relies on biogeochemical reanalysis corrected with Argo float data. Despite these
409 limitations linked to the models used here, we found that the seasonal variations of oxygen solubility and concentration
410 align with previous observational studies (Kress and Herut, 2001; Schlitzer et al., 1991). To provide a first quantitative
411 assessment of the contribution of various processes—air-sea flux, physical dynamics, and biogeochemical processes—
412 to oxygen budget, we chose an online and strictly closed budget approach. As shown by Trinh et al. (2024), this
413 approach can yield substantially higher accuracy than offline calculations, especially in the quantification of lateral
414 fluxes.

415 The model shows a net annual weak biological production of oxygen in the surface layer of the Levantine Basin,
416 primarily due to the sea's oligotrophic nature, which is more pronounced in the southeastern regions of the Levantine
417 Basin (D'Ortenzio, 2009; Lavigne et al., 2015). This oligotrophy is attributed to an anti-estuarine circulation
418 characterized by an eastward inflow of surface nutrient-depleted waters and an outflow of intermediate nutrient-rich
419 waters resulting from the water formation (Robinson and Golnaraghi, 1993). Interannual variability is nevertheless
420 observed here, with the sea being heterotrophic during mild winter years (2014 and 2018), consistent with the findings
421 by Mayot et al. (2016) using satellite ocean color data. By considering both surface and intermediate layers, the
422 Levantine Sea appears as a net heterotrophic system in the model results. This is in line with previous studies reporting
423 strong temporal and spatial heterogeneity in the trophic status of the oligotrophic Levantine Basin (Christaki et al.,
424 2011; Siokou-Frangou et al., 2010). The planktonic ecosystem is largely regulated by heterotrophic processes, with
425 higher heterotrophic/autotrophic biomass ratios typically observed in the most oligotrophic regions and during
426 stratified periods (Christaki et al., 2002; Siokou-Frangou et al., 2002). Despite this general heterotrophic character,
427 mesoscale physical structures promoting vertical mixing and nutrient upwelling play a key role in shaping the basin's
428 trophic gradients, particularly within cyclonic systems (Legendre and Rassoulzadegan, 1995; Salihoğlu et al., 1990).
429 Our model results show the high contribution of the Rhodes Gyre to the annual oxygen biological production in the
430 surface layer of the whole Levantine Basin area (around 41%). It has been identified as the major area of LIW
431 formation, characterising winter vertical mixing enriching the surface layer with nutrients and stimulating primary
432 production (D'Ortenzio et al., 2021; Lavigne et al., 2013). In the intermediate layer, biogeochemical fluxes in the Gyre

433 and the Levantine Basin exhibit little variation between mixing and stratification periods, especially during cold years,
434 consistent with the findings of Roether and Well (2001) and Klein et al. (2003).

435 The model indicates that the Levantine Basin absorbs atmospheric oxygen from November to April, while releasing
436 it during the rest of the year. This is in line with previous observational and modelling studies (Schlitzer et al. 1991,
437 Kress and Herut, 2001, Di Biagio et al. 2022). Except for the river-influenced areas (Nile river), the whole Levantine
438 Basin acts as an annual sink of atmospheric oxygen for all studied years, with an average uptake of $1.5 \pm 0.6 \text{ mol O}_2$
439 $\text{m}^{-2} \text{ yr}^{-1}$, and higher values during cold winter years. Uptake is enhanced in intermediate water formation areas, in
440 particular in the Rhodes Gyre, where undersaturation increases during winter due to stronger surface cooling and
441 mixing of poorer O_2 water masses with surface waters, in agreement with what was previously observed and modeled
442 in other water formation areas (Copin-Montégut and Bégovic, 2002; Coppola et al., 2017, 2018; Di Biagio et al., 2022;
443 Fourier et al., 2022; Körtzinger et al., 2004, 2008; Ulses et al., 2021; Wolf et al., 2018). The Rhodes Gyre shows a
444 comparable winter uptake rate ($20.3 \pm 7.4 \text{ mol O}_2 \text{ m}^{-2} \text{ yr}^{-1}$) as other water formation areas such as the Labrador Sea
445 and Gulf of Lion (ranging between 11 and $37 \text{ mol m}^{-2} \text{ yr}^{-1}$; Copin-Montégut & Bégovic, 2002; Coppola et al., 2017,
446 2018; Körtzinger et al., 2008; Ulses et al., 2021; Wolf et al., 2018). As a matter of comparison, the 7-year averaged
447 oxygen uptake estimated here for the whole Levantine Basin, characterized by relatively low solubility compared to
448 the rest of the Mediterranean (Mavropoulou et al., 2020, Di Biagio et al., 2022), represents 64% of the oxygen uptake
449 by the NW Mediterranean deep convection estimated for the cold year 2012-13 with the same coupled model (Ulses
450 et al., 2021). These estimates are nevertheless subject to methodological uncertainties. In particular, air-sea oxygen
451 fluxes depend on the parameterization of the gas transfer velocity, whose sensitivity to wind speed and formulation
452 can induce uncertainties of the order of 12-16%, as quantified by Ulses et al. (2021). Additional uncertainties arise
453 from surface heat flux estimates and the representation of vertical mixing, but these are not expected to modify the
454 relative importance or seasonal phasing of the dominant budget terms (Josey et al., 2013; Large et al., 1994).

455 Regarding vertical oxygen transport in the whole Levantine Basin, the weak upward transfer from the deep layer into
456 the intermediate layer found in our results is consistent with the general scheme of circulation or oxygen cycle shown
457 in previous studies (Mavropoulou et al., 2020; Powley et al., 2016; Roether and Schlitzer, 1991; Tanhua et al., 2013)
458 describing a gradual upwelling of deep water originating from the Adriatic Sea or Aegean Sea. While a downward
459 export of oxygen from the surface layer to the intermediate layer is simulated at the scale of the whole basin, the
460 Rhodes Gyre exhibits an opposite pattern, with oxygen being transported upward from the intermediate layers to the
461 surface. This upward input into the surface layer is balanced by a lateral export, particularly strong in winter, which
462 takes place notably through the dispersal by subduction of the newly formed LIW at the periphery of the mixed patch,
463 which is consistent with the observations reported by Malanotte-Rizzoli et al. (2003) for January 1995 during the
464 POEM cruise and by Taillandier et al. (2022) during PERLE cruises.

465 Finally, our results on lateral oxygen exchanges are also in agreement with previous studies describing the general
466 circulation in the Eastern Mediterranean Sea under BIOS cyclonic phases. During these cyclonic phases of the BIOS,
467 the cyclonic Northern Ionian Gyre promotes an important eastward advection of Atlantic Water toward the Levantine
468 Basin. As for the exchanges with the Ionian Sea, the general cyclonic circulation displays in the surface and
469 intermediate layers an eastward inflow along the Libyan-Egyptian coast (Estournel et al., 2021). South of Crete, the
470 flux reverses seasonally with an inflow from the Ionian in winter and an outflow in summer (Estournel et al., 2021).
471 The net oxygen flux directed from the Ionian toward the Levantine Basin in surface and intermediate waters in this

472 study results from a stronger southern input than the northern export at the Ionian-Levantine boundary. Regarding the
473 exchanges with the Aegean Sea, a net outflow of LSW and LIW by the Asia Minor Current through the Cretan Straits
474 was documented in several observational and modeling studies (Estournel et al., 2021; Millot and Taupier-Letage,
475 2005; Velaoras et al., 2014). During anticyclonic phases of the BIOS, the inflow from the Ionian Sea of Atlantic Water
476 is reduced and significant changes in oxygen circulation may be expected and deserve further investigation.

477 In addition, extreme events may episodically modulate air–sea oxygen exchanges in the Levantine Basin. In particular,
478 marine heatwaves, whose frequency and intensity have increased in the Eastern Mediterranean in recent decades
479 (Aboelkhair et al., 2023; Darmaraki et al., 2024), can enhance upper-ocean stratification, reduce vertical ventilation,
480 and decrease oxygen solubility through surface warming, potentially leading to transient oxygen anomalies in the
481 upper and intermediate layers (Keeling et al., 2010; Schmidtko et al., 2017). Moreover, Medicanes, short-lived and
482 spatially localized extreme events, could also impact biological dynamics and air-sea exchanges on their passage
483 (Menna et al., 2023; Jangir et al., 2024; Jangir et al., 2026; Reale et al., 2026). While a dedicated analysis of the
484 impacts of those extreme events (marine heatwaves, Medicanes) is beyond the scope of the present study, their effects
485 may contribute to short-term departures from the mean seasonal oxygen cycle and their integrated contribution to
486 basin-scale and annual oxygen budget will need to be assessed in future works.

487 Beyond the Levantine Basin, the processes identified here have broader implications for regional biogeochemical
488 dynamics and Earth system modelling. The quantified oxygen budget of LIW highlights the sensitivity of
489 intermediate-water ventilation to circulation and atmospheric forcing at seasonal to interannual timescales in semi-
490 enclosed basins (e.g. Tanhua et al., 2013; Schneider et al., 2014). Because LIW supplies the Eastern Intermediate
491 Water and flows in the whole Mediterranean basin, variability in its oxygen content may propagate in the other water
492 formation areas (South Aegean, South Adriatic, north-western Mediterranean), and as it constitutes the main precursor
493 of the Mediterranean Overflow Water, can influence the oxygen and biogeochemical properties of intermediate waters
494 beyond the Mediterranean in the Northeast Atlantic (Aldama-Campino & Döös, 2020; Stendardo and Gruber, 2012).
495 Accurately representing these processes is therefore essential for regional biogeochemical models and Earth system
496 models aiming to capture Mediterranean–Atlantic exchanges and their contribution to large-scale oxygen budgets.

497 **5 Conclusion and future works**

498 The study period was marked by contrasted atmospheric and hydrodynamic winter conditions. The confrontation of
499 the model results with cruise and BGC-Argo float observations shows the capacity of the model to capture the general
500 seasonal and spatial dissolved oxygen variability, as well as the main oxygen features in the Levantine Basin. These
501 in situ observations, particularly from BGC-Argo floats and ship-based measurements, were essential for constraining
502 and validating the simulations, without which the model outputs would not have reached their current level of
503 reliability. The following conclusions can be drawn:

- 504 - The model results indicate a clear seasonal cycle for the oxygen air-sea flux. During winter, with the decrease
505 in temperature, the increase in heat losses and intensified vertical mixing events, the surface layer is
506 undersaturated in oxygen, resulting in atmospheric oxygen uptake. Undersaturation averaged over the whole
507 basin reaches 2 % during winter. During the stratified period, primary production combined with the decrease
508 of the temperature-dependent solubility in the thin mixed layer above the SOM leads to oxygen oversaturation
509 and subsequent outgassing.

- 510 - At the annual scale, the Levantine Basin acts as a net sink for atmospheric oxygen, capturing 1.5 ± 0.6 mol
511 $\text{O}_2 \text{ m}^{-2} \text{ yr}^{-1}$ of oxygen. Most of the oxygen uptake occurs during winter, when it accounts for 10.7 ± 2.8 mol
512 $\text{O}_2 \text{ m}^{-2} \text{ yr}^{-1}$. The Rhodes Gyre absorbs atmospheric oxygen at a 2-fold higher rate than the entire Levantine
513 Basin.
- 514 - Our budget shows that the surface layer of the Levantine Basin is a net source of dissolved oxygen for the
515 intermediate waters, with winter vertical export of oxygen strongly modulated by the winter heat loss
516 intensity. Regarding the exchanges with the surrounding seas, we found that oxygen is laterally transported
517 into the Levantine Basin by surface and intermediate waters originating from the Ionian Sea. The lateral
518 annual oxygen outflow toward the Aegean Sea is strongly enhanced by the heat loss intensity with exports
519 1.5 and 2.4 times higher during cold years in the surface and intermediate layer, respectively, compared to
520 mild years.
- 521 - On an annual level, the Levantine Basin is found to act as a weak autotrophic ecosystem, with a net
522 community production in the surface layer alternating between auto- and heterotrophic status influenced by
523 the magnitude of the winter heat loss. In deeper depths and respiration resulted in an oxygen consumption of
524 2.0 ± 0.3 mol $\text{O}_2 \text{ m}^{-2} \text{ yr}^{-1}$. Spatially, the Rhodes Gyre appears to be a major oxygen reservoir across the basin,
525 contributing 41% of the oxygen production of the whole surface layer.

526 This study represents a first step in our modeling of the dissolved oxygen dynamics in the Levantine Basin. While the
527 quasi-permanent Rhodes Gyre dominates the basin-scale oxygen budget, transient cyclonic and anticyclonic
528 mesoscale structures are also expected to contribute to oxygen variability outside this gyre on shorter time scales, in
529 particular through nutrient upwelling or transport from nutrient-rich coastal waters offshore (Di Biagio et al., 2022;
530 Pirro et al., 2024). Further investigations focusing on the specific role of these various cyclonic and anticyclonic eddies
531 will be conducted in the future. Future work could also benefit from applying variability-based approaches, such as
532 empirical orthogonal function (EOF) or regime-oriented analyses on model fields, to further disentangle the respective
533 roles of physical and biogeochemical drivers across temporal scales (Di Biagio et al., 2023).

534 While the 7-year study period provides high-resolution insights into oxygen dynamics, it does not cover long-term
535 climate shifts such as the EMT. Several studies suggest a decadal variability of dissolved oxygen across the whole
536 water column linked to the dense water formations in the south Adriatic and Aegean seas and to the general eastern
537 Mediterranean circulation, notably the reversal of the North Ionian Gyre (Ozer et al., 2020, 2022). Extended the
538 simulation period, in addition to the implementation of a finer vertical resolution at key depths could contribute to
539 examining this longer-term variability in the Levantine Basin and the connections between the sub-basins of the
540 eastern Mediterranean. Improving the representation of intermediate water oxygen dynamics in the Mediterranean is
541 also a necessary step toward better quantifying Mediterranean–Atlantic biogeochemical coupling and its sensitivity to
542 future climate-driven changes in ventilation and circulation.

543 **In memoriam**

544 The authors wish to pay tribute to the memory of Pascal Conan, who passed away on August 5, 2025. He made
545 insightful contributions and was unwaveringly dedicated to biogeochemical oceanography. We will greatly miss him
546 both professionally and personally.

547 **Code availability**

548 The SYMPHONIE model and the MATLAB codes used to process the model outputs are available from the authors
549 on request.

550 **Data availability**

551 Data used to validate the model are available on different websites specified in the main text of the paper. These data
552 and the model outputs are also available from the authors on request.

553 **Author contributions**

554 CU, CE, and JH conceptualized the study. CE and PM ran the SYMPHONIE model. PM added the budget calculation
555 to the coupled model. CU and JH calibrated and ran the coupled physical–biogeochemical model. CE validated the
556 physical model, JH the biogeochemical model. Observational data were provided by PC, MPP, MaF, LC, CWR, DL
557 and TM. Funding acquisition was done by MiF, CU and CE. JH, CU, and CE wrote the initial version of the paper.
558 All authors contributed to the revision of the paper and approved the submitted version.

559 **Competing interests**

560 The contact author has declared that none of the authors has any competing interests.

561 **Acknowledgements**

562 This study is a contribution to the MerMex (Marine Ecosystem Response in the Mediterranean Experiment) project
563 of the MISTRALS international program. The numerical simulations were performed using the SYMPHONIE model,
564 developed by the Community Code SIROCCO (<https://sirocco.obs-mip.fr/>) coordinated by the Research Infrastructure
565 ILICO (CNRS-IFREMER) dedicated to coastal ocean observations (<https://www.ir-ilico.fr/?PagePrincipale>, last
566 access: 16 June 2025), and computed on the cluster of LAERO/OMP and HPC resources from CALMIP grants
567 (P1331). We acknowledge the scientists and crews of the Flotte océanographique française
568 (<https://www.flotteoceanographique.fr/>), who contributed to the cruises carried out in the framework of the PERLE
569 project. We thank Franck Dumas, chief scientist of the PERLE 1 campaign, for his role in organizing and leading the
570 cruise. The authors would like to acknowledge the National Council for Scientific Research of Lebanon (CNRS-L),
571 Campus France, the University of Toulouse, and LEGOS for granting a doctoral fellowship to Joelle Habib. We thank
572 Marta Álvarez (IEO, La Coruña) and collaborators for making the CARIMED database available to us.

573 **Financial support**

574 This research has been supported by the international programme MISTRALS (Marine Ecosystem Response in the
575 Mediterranean Experiment – MerMex; <https://www.odatis-ocean.fr/activites/activites-liees-aupole/chantiers/mistrals>, last access: 18 August 2025). The numerical simulations were performed with the
576 SYMPHONIE model developed by the Community Code SIROCCO (<https://sirocco.obs-mip.fr/>) and coordinated by
577 the Research Infrastructure ILICO (CNRS-IFREMER; <https://www.ir-ilico.fr/?PagePrincipale>, last access: 18 August
578 2025), with computational resources provided by the cluster of LAERO/OMP and CALMIP grants (P1331). The study
579

580 also received support from the National Council for Scientific Research of Lebanon (CNRS-L), Campus France, the
581 University of Toulouse, and LEGOS through a doctoral fellowship granted to Joelle Habib.

582 **References**

583 Aboelkhair, H., Mohamed, B., Morsy, M., and Nagy, H.: Co-occurrence of atmospheric and oceanic heatwaves in the
584 Eastern Mediterranean over the last four decades, *Remote Sens.*, 15, 1841, <https://doi.org/10.3390/rs15071841>, 2023.

585 Aldama-Campino, A., and Döös, K.: Mediterranean overflow water in the North Atlantic and its multidecadal
586 variability, *Tellus A: Dyn. Meteorol. Oceanogr.*, 72(1), 1–10, <https://doi.org/10.1080/16000870.2018.1565027>, 2020.

587 Álvarez, M., Velo, A., Tanhua, T., Key, R., and van Heuven, S.: CARBON, TRACER AND ANCILLARY DATA
588 IN THE MEDSEA, CARIMED: AN INTERNALLY CONSISTENT DATA PRODUCT FOR THE
589 MEDITERRANEAN SEA., 2019.

590 Arístegui, J., & UTM-CSIC. HOTMIX Cruise, RV Sarmiento de Gamboa [Data set]. UTM-CSIC.
591 <https://doi.org/10.20351/29SG20140427>, 2018.

592 Auger, P. A., Diaz, F., Ulses, C., Estournel, C., Neveux, J., Joux, F., Pujo-Pay, M., and Naudin, J. J.: Functioning of
593 the planktonic ecosystem on the Gulf of Lions shelf (NW Mediterranean) during spring and its impact on the carbon
594 deposition: a field data and 3-D modelling combined approach, *Biogeosciences*, 8, 3231–3261,
595 <https://doi.org/10.5194/bg-8-3231-2011>, 2011.

596 Auger, P. A., Ulses, C., Estournel, C., Stemmann, L., Somot, S., and Diaz, F.: Interannual control of plankton
597 communities by deep winter mixing and prey/predator interactions in the NW Mediterranean: Results from a 30-year
598 3D modeling study, *Prog. Oceanogr.*, 124, 12–27, <https://doi.org/10.1016/j.pocean.2014.04.004>, 2014.

599 Batistić, M., Garić, R., & Molinero, J. C.: Interannual variations in Adriatic Sea zooplankton mirror shifts in
600 circulation regimes in the Ionian Sea. *Climate research*, 61, 231-240, 2014.

601 Brasseur, P., Beckers, J. M., Brankart, J. M., and Schoenauer, R.: Seasonal temperature and salinity fields in the
602 Mediterranean Sea: Climatological analyses of a historical data set, *Deep Sea Res. Part Oceanogr. Res. Pap.*, 43, 159–
603 192, [https://doi.org/10.1016/0967-0637\(96\)00012-X](https://doi.org/10.1016/0967-0637(96)00012-X), 1996.

604 Cardin, V., Civitarese, G., Hainbucher, D., Bensi, M., and Rubino, A.: Thermohaline properties in the Eastern
605 Mediterranean in the last three decades: is the basin returning to the pre-EMT situation?, *Ocean Sci.*, 11, 53–66,
606 <https://doi.org/10.5194/os-11-53-2015>, 2015.

607 Christaki, U., Courties, C., Karayanni, H., Giannakourou, A., Maravelias, C., Kormas, K. Ar., and Lebaron, P.:
608 Dynamic Characteristics of Prochlorococcus and Synechococcus Consumption by Bacterivorous Nanoflagellates,
609 *Microb. Ecol.*, 43, 341–352, <https://doi.org/10.1007/s00248-002-2002-3>, 2002.

610 Christaki, U., Van Wambeke, F., Lefevre, D., Lagaria, A., Prieur, L., Pujo-Pay, M., Grattepanche, J.-D., Colombet,
611 J., Psarra, S., Dolan, J. R., Sime-Ngando, T., Conan, P., Weinbauer, M. G., and Moutin, T.: Microbial food webs and

612 metabolic state across oligotrophic waters of the Mediterranean Sea during summer, *Biogeosciences*, 8, 1839–1852,
613 <https://doi.org/10.5194/bg-8-1839-2011>, 2011.

614 Civitarese, G., Gačić, M., Batistić, M., Bensi, M., Cardin, V., Dulčić, J., and Menna, M.: The BIOS mechanism:
615 history, theory, implications, *Prog. Oceanogr.*, 216, 103056, <https://doi.org/10.1016/j.pocean.2023.103056>, 2023.

616 Civitarese, G., Gačić, M., Lipizer, M., and Eusebi Borzelli, G. L.: On the impact of the Bimodal Oscillating System
617 (BIOS) on the biogeochemistry and circulation of the Adriatic–Ionian system, *Prog. Oceanogr.*, 87, 1–10,
618 <https://doi.org/10.1016/j.pocean.2010.09.003>, 2010.

619 Conan, P. and Durrieu De Madron, X.: PERLE2 cruise, Pourquoi pas ? R/V, <https://doi.org/10.17600/18000865>, 2019.

620 Copin-Montégut, C. and Bégovic, M.: Distributions of carbonate properties and oxygen along the water column (0–
621 2000m) in the central part of the NW Mediterranean Sea (Dyfamed site): influence of winter vertical mixing on air–
622 sea CO₂ and O₂ exchanges, *Deep Sea Res. Part II Top. Stud. Oceanogr.*, 49, 2049–2066,
623 [https://doi.org/10.1016/S0967-0645\(02\)00027-9](https://doi.org/10.1016/S0967-0645(02)00027-9), 2002.

624 Coppola, L., Prieur, L., Taupier-Letage, I., Estournel, C., Testor, P., Lefevre, D., Belamari, S., LeReste, S., and
625 Taillandier, V.: Observation of oxygen ventilation into deep waters through targeted deployment of multiple A rgo-
626 O₂ floats in the north-western Mediterranean Sea in 2013, *J. Geophys. Res. Oceans*, 122, 6325–6341,
627 <https://doi.org/10.1002/2016JC012594>, 2017.

628 Coppola, L., Legendre, L., Lefevre, D., Prieur, L., Taillandier, V., and Diamond Riquier, E.: Seasonal and inter-annual
629 variations of dissolved oxygen in the northwestern Mediterranean Sea (DYFAMED site), *Prog. Oceanogr.*, 162, 187–
630 201, <https://doi.org/10.1016/j.pocean.2018.03.001>, 2018.

631 Cossarini, G., Feudale, L., Teruzzi, A., Bolzon, G., Coidessa, G., Solidoro, C., Di Biagio, V., Amadio, C., Lazzari, P.,
632 Brosich, A., and Salon, S.: High-Resolution Reanalysis of the Mediterranean Sea Biogeochemistry (1999–2019),
633 *Front. Mar. Sci.* 8, 741486, <https://doi.org/10.3389/fmars.2021.741486>, 2021.

634 Damien, P., Bosse, A., Testor, P., Marsaleix, P., and Estournel, C.: Modeling Postconvective Submesoscale Coherent
635 Vortices in the Northwestern Mediterranean Sea, *J. Geophys. Res. Oceans*, 122, 9937–9961,
636 <https://doi.org/10.1002/2016JC012114>, 2017.

637 Darmaraki, S., Denaxa, D., Theodorou, I., Livanou, E., Rigatou, D., Raitzos, E. D., Stavrakidis-Zachou, O.,
638 Dimarchopoulou, D., Bonino, G., McAdam, R., Organelli, E., Pitsouni, A., and Parasyris, A.: Marine heatwaves in
639 the Mediterranean Sea: A literature review, *Mediterr. Mar. Sci.*, 25(3), 586–620, <https://doi.org/10.12681/mms.38392>,
640 2024.

641 Di Biagio, V., Salon, S., Feudale, L., and Cossarini, G.: Subsurface oxygen maximum in oligotrophic marine
642 ecosystems: mapping the interaction between physical and biogeochemical processes, [https://doi.org/10.5194/bg-](https://doi.org/10.5194/bg-2022-70)
643 2022-70, 2022.

644 Di Biagio, V., Martellucci, R., Menna, M., Teruzzi, A., Amadio, C., Mauri, E., and Cossarini, G.: Dissolved oxygen
645 as an indicator of multiple drivers of the marine ecosystem: the southern Adriatic Sea case study, in: 7th edition of the

646 Copernicus Ocean State Report (OSR7), edited by: von Schuckmann, K., Moreira, L., Le Traon, P.-Y., Grégoire, M.,
647 Marcos, M., Staneva, J., Brasseur, P., Garric, G., Lionello, P., Karstensen, J., and Neukermans, G., Copernicus
648 Publications, State Planet, 1-osr7, 10, <https://doi.org/10.5194/sp-1-osr7-10-2023>, 2023.

649 D'Ortenzio, F. and Ribera d'Alcalà, M.: On the trophic regimes of the Mediterranean Sea: a satellite analysis,
650 *Biogeosciences*, 6, 139–148, <https://doi.org/10.5194/bg-6-139-2009>, 2009.

651 D'Ortenzio, F., Antoine, D., and Marullo, S.: Satellite-driven modeling of the upper ocean mixed layer and air–sea
652 CO₂ flux in the Mediterranean Sea, *Deep Sea Res. Part Oceanogr. Res. Pap.*, 55, 405–434,
653 <https://doi.org/10.1016/j.dsr.2007.12.008>, 2008.

654 D'Ortenzio, F., Taillandier, V., Claustre, H., Coppola, L., Conan, P., Dumas, F., Durrieu Du Madron, X., Fourier,
655 M., Gogou, A., Karageorgis, A., Lefevre, D., Leymarie, E., Oviedo, A., Pavlidou, A., Poteau, A., Poulain, P. M.,
656 Prieur, L., Psarra, S., Puyo-Pay, M., Ribera d'Alcalà, M., Schmechtig, C., Terrats, L., Velaoras, D., Wagener, T., and
657 Wimart-Rousseau, C.: BGC-Argo Floats Observe Nitrate Injection and Spring Phytoplankton Increase in the Surface
658 Layer of Levantine Sea (Eastern Mediterranean), *Geophys. Res. Lett.*, 48, e2020GL091649,
659 <https://doi.org/10.1029/2020GL091649>, 2021.

660 Escudier, R., Clementi, E., Cipollone, A., Pistoia, J., Drudi, M., Grandi, A., Lyubartsev, V., Lecci, R., Aydogdu, A.,
661 Delrosso, D., Omar, M., Masina, S., Coppini, G., and Pinardi, N.: A High Resolution Reanalysis for the Mediterranean
662 Sea, *Front. Earth Sci.*, 9, 702285, <https://doi.org/10.3389/feart.2021.702285>, 2021.

663 Estournel, C., Kondrachoff, V., Marsaleix, P., and Vehil, R.: The plume of the Rhone: numerical simulation and
664 remote sensing, *Cont. Shelf Res.*, 17, 899–924, [https://doi.org/10.1016/S0278-4343\(96\)00064-7](https://doi.org/10.1016/S0278-4343(96)00064-7), 1997.

665 Estournel, C., Broche, P., Marsaleix, P., Devenon, J.-L., Auclair, F., and Vehil, R.: The Rhone River Plume in
666 Unsteady Conditions: Numerical and Experimental Results, *Estuar. Coast. Shelf Sci.*, 53, 25–38,
667 <https://doi.org/10.1006/ecss.2000.0685>, 2001.

668 Estournel, C., Zervakis, V., Marsaleix, P., Papadopoulos, A., Auclair, F., Perivoliotis, L., and Tragou, E.: Dense water
669 formation and cascading in the Gulf of Thermaikos (North Aegean), from observations and modelling, *Cont. Shelf
670 Res.*, 25, 2366–2386, <https://doi.org/10.1016/j.csr.2005.08.014>, 2005.

671 Estournel, C., Testor, P., Damien, P., D'Ortenzio, F., Marsaleix, P., Conan, P., Kessouri, F., Durrieu De Madron, X.,
672 Coppola, L., Lellouche, J., Belamari, S., Mortier, L., Ulses, C., Bouin, M., and Prieur, L.: High resolution modeling
673 of dense water formation in the north-western Mediterranean during winter 2012–2013: Processes and budget, *J.
674 Geophys. Res. Oceans*, 121, 5367–5392, <https://doi.org/10.1002/2016JC011935>, 2016.

675 Estournel, C., Marsaleix, P., and Ulses, C.: A new assessment of the circulation of Atlantic and Intermediate Waters
676 in the Eastern Mediterranean, *Prog. Oceanogr.*, 198, 102673, <https://doi.org/10.1016/j.pocean.2021.102673>, 2021.

677 Fach, B. A., Örek, H., Salihoglu, I., Tezcan, D., Latif, M. A., and Salihoğlu, B.: Water mass variability and Levantine
678 Intermediate Water formation in the eastern Mediterranean between 2015 and 2017, *J. Geophys. Res. Oceans*, 126,
679 e2020JC016472, <https://doi.org/10.1029/2020JC016472>, 2021

680 Feucher, C., Portela, E., Kolodziejczyk, N., and Thierry, V.: Subpolar gyre decadal variability explains the recent
681 oxygenation in the Irminger Sea, *Commun. Earth Environ.*, **3**, 279, <https://doi.org/10.1038/s43247-022-00570-y>, 2022

682 Fourier, M.: Dataset used for CANYON-MED training and validation,
683 <https://doi.org/10.6084/M9.FIGSHARE.12452795.V2>, 2020.

684 Fourier, M., Coppola, L., D’Ortenzio, F., Migon, C., and Gattuso, J.: Impact of Intermittent Convection in the
685 Northwestern Mediterranean Sea on Oxygen Content, Nutrients, and the Carbonate System, *J. Geophys. Res. Oceans*,
686 **127**, e2022JC018615, <https://doi.org/10.1029/2022JC018615>, 2022.

687 Gačić, M., Borzelli, G. L. E., Civitarese, G., Cardin, V., and Yari, S.: Can internal processes sustain reversals of the
688 ocean upper circulation? The Ionian Sea example, *Geophys. Res. Lett.*, **37**, 2010GL043216,
689 <https://doi.org/10.1029/2010GL043216>, 2010.

690 Garinet, A., Herrmann, M., Marsaleix, P., and Pénicaud, J.: Spurious numerical mixing under strong tidal forcing: a
691 case study in the south-east Asian seas using the Symphonie model (v3.1.2), *Geosci. Model Dev.*, **17**, 6967–6986,
692 <https://doi.org/10.5194/gmd-17-6967-2024>, 2024.

693 Grégoire, M., Raick, C., and Soetaert, K.: Numerical modeling of the central Black Sea ecosystem functioning during
694 the eutrophication phase, *Prog. Oceanogr.*, **76**, 286–333, <https://doi.org/10.1016/j.pocean.2008.01.002>, 2008.

695 Grégoire, M., Garçon, V., Garcia, H., Breitburg, D., Isensee, K., Oschlies, A., Telszewski, M., Barth, A., Bittig, H.
696 C., Carstensen, J., Carval, T., Chai, F., Chavez, F., Conley, D., Coppola, L., Crowe, S., Currie, K., Dai, M., Deflandre,
697 B., Dewitte, B., Diaz, R., Garcia-Robledo, E., Gilbert, D., Giorgetti, A., Glud, R., Gutierrez, D., Hosoda, S., Ishii, M.,
698 Jacinto, G., Langdon, C., Lauvset, S. K., Levin, L. A., Limburg, K. E., Mehrtens, H., Montes, I., Naqvi, W., Paulmier,
699 A., Pfeil, B., Pitcher, G., Pouliquen, S., Rabalais, N., Rabouille, C., Recape, V., Roman, M., Rose, K., Rudnick, D.,
700 Rummer, J., Schmechtig, C., Schmidtko, S., Seibel, B., Slomp, C., Sumalia, U. R., Tanhua, T., Thierry, V., Uchida,
701 H., Wanninkhof, R., and Yasuhara, M.: A Global Ocean Oxygen Database and Atlas for Assessing and Predicting
702 Deoxygenation and Ocean Health in the Open and Coastal Ocean, *Front. Mar. Sci.*, **8**, 724913,
703 <https://doi.org/10.3389/fmars.2021.724913>, 2021.

704 Habib, J., Ulses, C., Estournel, C., Fakhri, M., Marsaleix, P., Pujo-Pay, M., Fourier, M., Coppola, L., Mignot, A.,
705 Mortier, L., and Conan, P.: Seasonal and interannual variability of the pelagic ecosystem and of the organic carbon
706 budget in the Rhodes Gyre (eastern Mediterranean): influence of winter mixing, *Biogeosciences*, **20**, 3203–3228,
707 <https://doi.org/10.5194/bg-20-3203-2023>, 2023.

708 Hainbucher, D., Álvarez, M., Astray Uceda, B., Bachi, G., Cardin, V., Celentano, P., Chaikakis, S., Chavez Montero,
709 M. D. M., Civitarese, G., Fajar, N. M., Fripiat, F., Gerke, L., Gogou, A., Fernández Guallart, E., Gülk, B., Hassoun,
710 A. E. R., Lange, N., Rochner, A., Santinelli, C., Steinhoff, T., Tanhua, T., Urbini, L., Velaoras, D., Wolf, F., and
711 Welsch, A.: Variability and Trends in Physical and Biogeochemical Parameters of the Mediterranean Sea during a
712 Cruise with RV MARIA S. MERIAN in March 2018, <https://doi.org/10.5194/essd-2020-82>, 7 July 2020.

713 Helm, K. P., Bindoff, N. L., and Church, J. A.: Observed decreases in oxygen content of the global ocean: Global
714 decreases in ocean oxygen levels, *Geophys. Res. Lett.*, **38**, n/a-n/a, <https://doi.org/10.1029/2011GL049513>, 2011.

715 Herrmann, M., Somot, S., Sevault, F., Estournel, C., and Déqué, M.: Modeling the deep convection in the northwestern
716 Mediterranean Sea using an eddy-permitting and an eddy-resolving model: Case study of winter 1986–1987, *J.*
717 *Geophys. Res. Oceans*, 113, 2006JC003991, <https://doi.org/10.1029/2006JC003991>, 2008.

718 Herrmann, M., Diaz, F., Estournel, C., Marsaleix, P., and Ulses, C.: Impact of atmospheric and oceanic interannual
719 variability on the Northwestern Mediterranean Sea pelagic planktonic ecosystem and associated carbon cycle:
720 Interannual Variability Impact on Nwms, *J. Geophys. Res. Oceans*, 118, 5792–5813,
721 <https://doi.org/10.1002/jgrc.20405>, 2013.

722 Houpert, L., Testor, P., Durrieu De Madron, X., Somot, S., D’Ortenzio, F., Estournel, C., and Lavigne, H.: Seasonal
723 cycle of the mixed layer, the seasonal thermocline and the upper-ocean heat storage rate in the Mediterranean Sea
724 derived from observations, *Prog. Oceanogr.*, 132, 333–352, <https://doi.org/10.1016/j.pocean.2014.11.004>, 2015.

725 Jangir, B., Mishra, A. K., and Strobach, E.: The interplay between medicanes and the Mediterranean Sea in the
726 presence of sea surface temperature anomalies, *Atmos. Res.*, 310, 107625,
727 <https://doi.org/10.1016/j.atmosres.2024.107625>, 2024.

728 Jangir, B., Reale, M., Menna, M., Mishra, A. K., Marellucci, R., Cossarini, G., et al.: The response of the physical and
729 biogeochemical marine environment to the passage of Mediterranean cyclones in the presence of eddies, gyres, and
730 marine heat waves, *J. Geophys. Res. Oceans*, 131, e2025JC023151, doi:10.1029/2025JC023151, 2026.

731 Josey, S. A., Gulev, S., and Yu, L.: Exchanges through the ocean surface, in: *Ocean Circulation and Climate*, 2nd
732 edn., edited by: Siedler, G., Griffies, S. M., Gould, J., and Church, J. A., Academic Press, 115–140,
733 <https://doi.org/10.1016/B978-0-12-391851-2.00005-2>, 2013.

734 Keeling, R. F., Körtzinger, A., and Gruber, N.: Ocean deoxygenation in a warming world, *Annu. Rev. Mar. Sci.*, 2,
735 199–229, <https://doi.org/10.1146/annurev.marine.010908.163855>, 2010.

736 Kessouri, F., Ulses, C., Estournel, C., Marsaleix, P., Severin, T., Pujo-Pay, M., Caparros, J., Raimbault, P., Pasqueron
737 De Fommervault, O., D’Ortenzio, F., Taillandier, V., Testor, P., and Conan, P.: Nitrogen and Phosphorus Budgets in
738 the Northwestern Mediterranean Deep Convection Region, *J. Geophys. Res. Oceans*, 122, 9429–9454,
739 <https://doi.org/10.1002/2016JC012665>, 2017.

740 Kessouri, F., Ulses, C., Estournel, C., Marsaleix, P., D’Ortenzio, F., Severin, T., Taillandier, V., and Conan, P.:
741 Vertical Mixing Effects on Phytoplankton Dynamics and Organic Carbon Export in the Western Mediterranean Sea,
742 *J. Geophys. Res. Oceans*, 123, 1647–1669, <https://doi.org/10.1002/2016JC012669>, 2018.

743 Klein, B., Roether, W., Kress, N., Manca, B. B., Ribera d’Alcala, M., Souvermezoglou, E., Theocharis, A., Civitarese,
744 G., and Luchetta, A.: Accelerated oxygen consumption in eastern Mediterranean deep waters following the recent
745 changes in thermohaline circulation, *J. Geophys. Res. Oceans*, 108, 2002JC001454,
746 <https://doi.org/10.1029/2002JC001454>, 2003.

747 Kolodziejczyk, N., Portela, E., Thierry, V., and Prigent, A.: ISASO2: recent trends and regional patterns of ocean
748 dissolved oxygen change, *Earth Syst. Sci. Data*, 16, 5191–5206, <https://doi.org/10.5194/essd-16-5191-2024>, 2024.

749 Körtzinger, A., Schimanski, J., Send, U., and Wallace, D.: The Ocean Takes a Deep Breath, *Science*, 306, 1337–1337,
750 <https://doi.org/10.1126/science.1102557>, 2004.

751 Körtzinger, A., Send, U., Lampitt, R. S., Hartman, S., Wallace, D. W. R., Karstensen, J., Villagarcia, M. G., Llinás,
752 O., and DeGrandpre, M. D.: The seasonal p CO₂ cycle at 49°N/16.5°W in the northeastern Atlantic Ocean and what
753 it tells us about biological productivity, *J. Geophys. Res. Oceans*, 113, 2007JC004347,
754 <https://doi.org/10.1029/2007JC004347>, 2008.

755 Kress, N. and Herut, B.: Spatial and seasonal evolution of dissolved oxygen and nutrients in the Southern Levantine
756 Basin (Eastern Mediterranean Sea): chemical characterization of the water masses and inferences on the N:P ratios,
757 *Deep Sea Res. Part Oceanogr. Res. Pap.*, 48, 2347–2372, [https://doi.org/10.1016/S0967-0637\(01\)00022-X](https://doi.org/10.1016/S0967-0637(01)00022-X), 2001.

758 Kress, N., Manca, B. B., Klein, B., and Deponte, D.: Continuing influence of the changed thermohaline circulation in
759 the eastern Mediterranean on the distribution of dissolved oxygen and nutrients: Physical and chemical
760 characterization of the water masses, *J. Geophys. Res. Oceans*, 108, 2002JC001397,
761 <https://doi.org/10.1029/2002JC001397>, 2003.

762 Kress, N., Gertman, I., and Herut, B.: Temporal evolution of physical and chemical characteristics of the water column
763 in the Easternmost Levantine basin (Eastern Mediterranean Sea) from 2002 to 2010, *J. Mar. Syst.*, 135, 6–13,
764 <https://doi.org/10.1016/j.jmarsys.2013.11.016>, 2014.

765 Lagaria, A., Psarra, S., Lefèvre, D., Van Wambeke, F., Courties, C., Pujo-Pay, M., Oriol, L., Tanaka, T., and Christaki,
766 U.: The effects of nutrient additions on particulate and dissolved primary production and metabolic state in surface
767 waters of three Mediterranean eddies, *Biogeosciences*, 8, 2595–2607, <https://doi.org/10.5194/bg-8-2595-2011>, 2011.

768 Large, W. G., McWilliams, J. C., and Doney, S. C.: Oceanic vertical mixing: A review and a model with a nonlocal
769 boundary layer parameterization, *Rev. Geophys.*, 32, 363–403, <https://doi.org/10.1029/94RG01872>, 1994.

770 Lascaratos, A. and Nittis, K.: A high-resolution three-dimensional numerical study of intermediate water formation in
771 the Levantine Sea, *J. Geophys. Res. Oceans*, 103, 18497–18511, <https://doi.org/10.1029/98JC01196>, 1998.

772 Lascaratos, A., Roether, W., Nittis, K., and Klein, B.: Recent changes in deep water formation and spreading in the
773 eastern Mediterranean Sea: a review, *Prog. Oceanogr.*, 44, 5–36, [https://doi.org/10.1016/S0079-6611\(99\)00019-1](https://doi.org/10.1016/S0079-6611(99)00019-1),
774 1999.

775 Lavigne, H., D’Ortenzio, F., Migon, C., Claustre, H., Testor, P., d’Alcalà, M. R., Lavezza, R., Houpert, L., and Prieur,
776 L.: Enhancing the comprehension of mixed layer depth control on the Mediterranean phytoplankton phenology:
777 Mediterranean Phytoplankton Phenology, *J. Geophys. Res. Oceans*, 118, 3416–3430,
778 <https://doi.org/10.1002/jgrc.20251>, 2013.

779 Lavigne, H., D’Ortenzio, F., Ribera D’Alcalà, M., Claustre, H., Sauzède, R., and Gacic, M.: On the vertical
780 distribution of the chlorophyll a concentration in the Mediterranean Sea: a basin-scale and seasonal approach,
781 *Biogeosciences*, 12, 5021–5039, <https://doi.org/10.5194/bg-12-5021-2015>, 2015.

782 Legendre, L. and Rassoulzadegan, F.: Plankton and nutrient dynamics in marine waters, *Ophelia*, 41, 153–172,
783 <https://doi.org/10.1080/00785236.1995.10422042>, 1995.

784 Malanotte-Rizzoli, P., Manca, B. B., Marullo, S., Ribera D'Alcala', M., Roether, W., Theocharis, A., Bergamasco,
785 A., Budillon, G., Sansone, E., Civitarese, G., Conversano, F., Gertman, I., Hernt, B., Kress, N., Kioroglou, S.,
786 Kontoyannis, H., Nittis, K., Klein, B., Lascaratos, A., Latif, M. A., Ozsoy, E., Robinson, A. R., Santoleri, R., Viezzoli,
787 D., and Kovacevic, V.: The Levantine Intermediate Water Experiment (LIWEX) Group: Levantine basin—A
788 laboratory for multiple water mass formation processes, *J. Geophys. Res. Oceans*, 108, 2002JC001643,
789 <https://doi.org/10.1029/2002JC001643>, 2003.

790 Malanotte-Rizzoli, P., Artale, V., Borzelli-Eusebi, G. L., Brenner, S., Crise, A., Gacic, M., Kress, N., Marullo, S.,
791 Ribera d'Alcalà, M., Sofianos, S., Tanhua, T., Theocharis, A., Alvarez, M., Ashkenazy, Y., Bergamasco, A., Cardin,
792 V., Carniel, S., Civitarese, G., D'Ortenzio, F., Font, J., Garcia-Ladona, E., Garcia-Lafuente, J. M., Gogou, A.,
793 Gregoire, M., Hainbucher, D., Kontoyannis, H., Kovacevic, V., Kraskapoulou, E., Kroskos, G., Incarbona, A.,
794 Mazzocchi, M. G., Orlic, M., Ozsoy, E., Pascual, A., Poulain, P.-M., Roether, W., Rubino, A., Schroeder, K., Siokou-
795 Frangou, J., Souvermezoglou, E., Sprovieri, M., Tintoré, J., and Triantafyllou, G.: Physical forcing and
796 physical/biochemical variability of the Mediterranean Sea: a review of unresolved issues and directions for future
797 research, *Ocean Sci.*, 10, 281–322, <https://doi.org/10.5194/os-10-281-2014>, 2014.

798 Manca, B., Burca, M., Giorgetti, A., Coatanoan, C., Garcia, M.-J., and Iona, A.: Physical and biochemical averaged
799 vertical profiles in the Mediterranean regions: an important tool to trace the climatology of water masses and to
800 validate incoming data from operational oceanography, *J. Mar. Syst.*, 48, 83–116,
801 <https://doi.org/10.1016/j.jmarsys.2003.11.025>, 2004.

802 Manca, B. B., Ibello, V., Pacciaroni, M., Scarazzato, P., & Giorgetti, A.: Ventilation of deep waters in the Adriatic
803 and Ionian Seas following changes in thermohaline circulation of the Eastern Mediterranean. *Climate Research*, 31,
804 239-256, 2006.

805 Many, G., Ulses, C., Estournel, C., and Marsaleix, P.: Particulate organic carbon dynamics in the Gulf of Lion shelf
806 (NW Mediterranean) using a coupled hydrodynamic–biogeochemical model, *Biogeosciences*, 18, 5513–5538,
807 <https://doi.org/10.5194/bg-18-5513-2021>, 2021.

808 Marsaleix, P., Estournel, C., Kondrachoff, V., and Vehil, R.: A numerical study of the formation of the Rhône River
809 plume, *J. Mar. Syst.*, 14, 99–115, [https://doi.org/10.1016/S0924-7963\(97\)00011-0](https://doi.org/10.1016/S0924-7963(97)00011-0), 1998.

810 Marsaleix, P., Auclair, F., and Estournel, C.: Considerations on Open Boundary Conditions for Regional and Coastal
811 Ocean Models, *J. Atmospheric Ocean. Technol.*, 23, 1604–1613, <https://doi.org/10.1175/JTECH1930.1>, 2006.

812 Marsaleix, P., Auclair, F., Floor, J. W., Herrmann, M. J., Estournel, C., Pairaud, I., and Ulses, C.: Energy conservation
813 issues in sigma-coordinate free-surface ocean models, *Ocean Model.*, 20, 61–89,
814 <https://doi.org/10.1016/j.ocemod.2007.07.005>, 2008.

815 Martínez-Pérez, A. M., Osterholz, H., Nieto-Cid, M., Álvarez, M., Dittmar, T., and Álvarez-Salgado, X. A.: Molecular
816 composition of dissolved organic matter in the Mediterranean Sea, *Limnol. Oceanogr.*, 62, 2699–2712,
817 <https://doi.org/10.1002/lno.10600>, 2017.

818 Mavropoulou, A.-M., Vervatis, V., and Sofianos, S.: Dissolved oxygen variability in the Mediterranean Sea, *J. Mar.*
819 *Syst.*, 208, 103348, <https://doi.org/10.1016/j.jmarsys.2020.103348>, 2020.

820 Mayot, N., D’Ortenzio, F., Ribera d’Alcalà, M., Lavigne, H., and Claustre, H.: Interannual variability of the
821 Mediterranean trophic regimes from ocean color satellites, *Biogeosciences*, 13, 1901–1917,
822 <https://doi.org/10.5194/bg-13-1901-2016>, 2016.

823 Menna, M., Martellucci, R., Reale, M., Cossarini, G., Salon, S., Notarstefano, G., et al. (2023). A case study of impacts
824 of an extreme weather system on the Mediterranean Sea circulation features: Medicane Apollo (2021). *Scientific*
825 *Reports*, 13(1), 3870. <https://doi.org/10.1038/s41598-023-29942-w>

826 Menna, M., Poulain, P.-M., Zodiatis, G., and Gertman, I.: On the decadal variability of the North Ionian Gyre and its
827 impact on the thermohaline properties of the Levantine Intermediate Water, *Prog. Oceanogr.*, 200, 102709,
828 <https://doi.org/10.1016/j.pocean.2021.102709>, 2022.

829 Mikolajczak, G., Estournel, C., Ulses, C., Marsaleix, P., Bourrin, F., Martín, J., Pairaud, I., Puig, P., Leredde, Y.,
830 Many, G., Seyfried, L., and Durrieu De Madron, X.: Impact of storms on residence times and export of coastal waters
831 during a mild autumn/winter period in the Gulf of Lion, *Cont. Shelf Res.*, 207, 104192,
832 <https://doi.org/10.1016/j.csr.2020.104192>, 2020.

833 Millot, C. and Taupier-Letage, I.: Circulation in the Mediterranean Sea, in: *The Mediterranean Sea*, vol. 5K, edited
834 by: Salot, A., Springer Berlin Heidelberg, Berlin, Heidelberg, 29–66, <https://doi.org/10.1007/b107143>, 2005.

835 Moutin, T. and Raimbault, P.: Primary production, carbon export and nutrients availability in western and eastern
836 Mediterranean Sea in early summer 1996 (MINOS cruise), *J. Marine Syst.*, 33–34, 273–288,
837 [https://doi.org/10.1016/S0924-7963\(02\)00062-3](https://doi.org/10.1016/S0924-7963(02)00062-3), 2002

838 Ozer, T., Gertman, I., Kress, N., Silverman, J., and Herut, B.: Interannual thermohaline (1979–2014) and nutrient
839 (2002–2014) dynamics in the Levantine surface and intermediate water masses, SE Mediterranean Sea, *Glob. Planet.*
840 *Change*, 151, 60–67, <https://doi.org/10.1016/j.gloplacha.2016.04.001>, 2016.

841 Ozer, T., Gertman, I., Gildor, H., Goldman, R., and Herut, B.: Evidence for recent thermohaline variability and
842 processes in the deep water of the Southeastern Levantine Basin, Mediterranean Sea, *Deep Sea Res. Part II Top. Stud.*
843 *Oceanogr.*, 171, 104651, <https://doi.org/10.1016/j.dsr2.2019.104651>, 2020.

844 Ozer, T., Rahav, E., Gertman, I., Sisma-Ventura, G., Silverman, J., and Herut, B.: Relationship between thermohaline
845 and biochemical patterns in the levantine upper and intermediate water masses, Southeastern Mediterranean Sea
846 (2013–2021), *Front. Mar. Sci.*, 9, 958924, <https://doi.org/10.3389/fmars.2022.958924>, 2022.

847 Pirro, A., Menna, M., Mauri, E., Laxenaire, R., Salon, S., Bosse, A., Martellucci, R., Viboud, S., Valran, T., Hayes,
848 D., Speich, S., Poulain, P.-M., and Negretti, M. E.: Rossby waves driven by the Mid Mediterranean Jet impact the
849 Eastern Mediterranean mesoscale dynamics, *Sci. Rep.*, **14**, 29598, <https://doi.org/10.1038/s41598-024-80293-6>, 2024.

850 Powley, H. R., Krom, M. D., and Van Cappellen, P.: Circulation and oxygen cycling in the Mediterranean Sea:
851 Sensitivity to future climate change: OXYGEN CYCLING IN THE MEDITERRANEAN SEA, *J. Geophys. Res.*
852 *Oceans*, **121**, 8230–8247, <https://doi.org/10.1002/2016JC012224>, 2016.

853 Reale, M., Giordano, F., Biagio, V. D., Cossarini, G., & Salon, S. (2026). Synoptic features driving the CO₂ sink in
854 the Mediterranean Sea in winter. *Journal of Geophysical Research: Atmospheres*, **131**(2), e2025JD044310.
855 <https://doi.org/10.1029/2025JD044310>

856 Regaudie-de-Gioux, A., Vaquer-Sunyer, R., and Duarte, C. M.: Patterns in planktonic metabolism in the
857 Mediterranean Sea, 2009.

858 Robinson, A. R. and Golnaraghi, M.: Circulation and dynamics of the Eastern Mediterranean Sea; quasi-synoptic data-
859 driven simulations, *Deep Sea Res. Part II Top. Stud. Oceanogr.*, **40**, 1207–1246, <https://doi.org/10.1016/0967->
860 [0645\(93\)90068-X](https://doi.org/10.1016/0967-0645(93)90068-X), 1993.

861 Roether, W. and Schlitzer, R.: Eastern Mediterranean deep water renewal on the basis of chlorofluoromethane and
862 tritium data, *Dyn. Atmospheres Oceans*, **15**, 333–354, [https://doi.org/10.1016/0377-0265\(91\)90025-B](https://doi.org/10.1016/0377-0265(91)90025-B), 1991.

863 Roether, W. and Well, R.: Oxygen consumption in the Eastern Mediterranean, *Deep Sea Res. Part Oceanogr. Res.*
864 *Pap.*, **48**, 1535–1551, [https://doi.org/10.1016/S0967-0637\(00\)00102-3](https://doi.org/10.1016/S0967-0637(00)00102-3), 2001.

865 Salihoğlu, İ., Saydam, C., Baştürk, Ö., Yılmaz, K., Göçmen, D., Hatipoğlu, E., and Yılmaz, A.: Transport and
866 distribution of nutrients and chlorophyll-a by mesoscale eddies in the northeastern Mediterranean, *Mar. Chem.*, **29**,
867 **375–390**, [https://doi.org/10.1016/0304-4203\(90\)90024-7](https://doi.org/10.1016/0304-4203(90)90024-7), 1990.

868 Schlitzer, R., Roether, W., Oster, H., Junghans, H.-G., Hausmann, M., Johannsen, H., and Michelato, A.:
869 Chlorofluoromethane and oxygen in the Eastern Mediterranean, *Deep Sea Res. Part Oceanogr. Res. Pap.*, **38**, 1531–
870 **1551**, [https://doi.org/10.1016/0198-0149\(91\)90088-W](https://doi.org/10.1016/0198-0149(91)90088-W), 1991.

871 Schmidtko, S., Stramma, L., and Visbeck, M.: Decline in global oceanic oxygen content during the past five decades,
872 *Nature*, **542**, 335–339, <https://doi.org/10.1038/nature21399>, 2017.

873 Schneider, A., Tanhua, T., Roether, W., and Steinfeldt, R.: Changes in ventilation of the Mediterranean Sea during
874 the past 25 year, *Ocean Sci.*, **10**, 1–16, <https://doi.org/10.5194/os-10-1-2014>, 2014.

875 Siokou-Frangou, I., Bianchi, M., Christaki, U., Christou, E. D., Giannakourou, A., Gotsis, O., Ignatiades, L., Pagou,
876 K., Pitta, P., Psarra, S., Souvermezoglou, E., Van Wambeke, F., and Zervakis, V.: Carbon flow in the planktonic food
877 web along a gradient of oligotrophy in the Aegean Sea (Mediterranean Sea), *J. Mar. Syst.*, **33–34**, 335–353,
878 [https://doi.org/10.1016/S0924-7963\(02\)00065-9](https://doi.org/10.1016/S0924-7963(02)00065-9), 2002.

879 Siokou-Frangou, I., Christaki, U., Mazzocchi, M. G., Montresor, M., Ribera d'Alcalá, M., Vaqué, D., and Zingone,
880 A.: Plankton in the open Mediterranean Sea: a review, *Biogeosciences*, 7, 1543–1586, [https://doi.org/10.5194/bg-7-](https://doi.org/10.5194/bg-7-1543-2010)
881 1543-2010, 2010.

882 Sisma-Ventura, G., Yam, R., Kress, N., and Shemesh, A.: Water column distribution of stable isotopes and carbonate
883 properties in the South-eastern Levantine basin (Eastern Mediterranean): Vertical and temporal change, *J. Mar. Syst.*,
884 158, 13–25, <https://doi.org/10.1016/j.jmarsys.2016.01.012>, 2016.

885 Sisma-Ventura, G., Kress, N., Silverman, J., Gertner, Y., Ozer, T., Biton, E., Lazar, A., Gertman, I., Rahav, E., and
886 Herut, B.: Post-eastern Mediterranean Transient Oxygen Decline in the Deep Waters of the Southeast Mediterranean
887 Sea Supports Weakening of Ventilation Rates, *Front. Mar. Sci.* 7, 598686, <https://doi.org/10.3389/fmars.2020.598686>,
888 2021.

889 Stendardo, I., and Gruber, N.: Oxygen trends over five decades in the North Atlantic, *J. Geophys. Res. Oceans*, 117,
890 C11004, <https://doi.org/10.1029/2012JC007909>, 2012.

891 Stramma, L. and Schmidtko, S.: Spatial and Temporal Variability of Oceanic Oxygen Changes and Underlying
892 Trends, *Atmosphere-Ocean*, 59, 122–132, <https://doi.org/10.1080/07055900.2021.1905601>, 2021.

893 Sur, H., Ozsoy, E., and Unluata, U.: Simultaneous deep and intermediate depth convection in the northern levantine
894 sea, winter 1992, *Oceanol. Acta*, 16, 1993.

895 Tanhua, T.: Hydrochemistry of water samples during METEOR cruise M83/1,
896 <https://doi.org/10.1594/PANGAEA.821729>, 2013.

897 Tanhua, T., Hainbucher, D., Schroeder, K., Cardin, V., Álvarez, M., and Civitarese, G.: The Mediterranean Sea
898 system: a review and an introduction to the special issue, *Ocean Sci.*, 9, 789–803, [https://doi.org/10.5194/os-9-789-](https://doi.org/10.5194/os-9-789-2013)
899 2013, 2013.

900 Thierry, V., Bittig, H., and The Argo-Bgc Team: Argo quality control manual for dissolved oxygen concentration,
901 Argo-BGC group, <https://doi.org/10.13155/46542>, 2021.

902 Trinh, N. B., Herrmann, M., Ulses, C., Marsaleix, P., Duhaut, T., To Duy, T., Estournel, C., and Shearman, R. K.:
903 New insights into the South China Sea throughflow and water budget seasonal cycle: evaluation and analysis of a
904 high-resolution configuration of the ocean model SYMPHONIE version 2.4, *Geosci. Model Dev.*, 17, 1831–1867,
905 <https://doi.org/10.5194/gmd-17-1831-2024>, 2024.

906 Tugrul, S., Besiktepe, T., and Salihoglu, I.: Nutrient exchange fluxes between the Aegean and Black Seas through the
907 Marmara Sea, *Mediterr. Mar. Sci.*, 3, 33, <https://doi.org/10.12681/mms.256>, 2002.

908 Ulses, C., Estournel, C., Puig, P., Durrieu De Madron, X., and Marsaleix, P.: Dense shelf water cascading in the
909 northwestern Mediterranean during the cold winter 2005: Quantification of the export through the Gulf of Lion and
910 the Catalan margin, *Geophys. Res. Lett.*, 35, 2008GL033257, <https://doi.org/10.1029/2008GL033257>, 2008.

911 Ulses, C., Auger, P. -A., Soetaert, K., Marsaleix, P., Diaz, F., Coppola, L., Herrmann, M. J., Kessouri, F., and
912 Estournel, C.: Budget of organic carbon in the North- Western Mediterranean open sea over the period 2004–2008
913 using 3-D coupled physical-biogeochemical modeling, *J. Geophys. Res. Oceans*, 121, 7026–7055,
914 <https://doi.org/10.1002/2016JC011818>, 2016.

915 Ulses, C., Estournel, C., Fourier, M., Coppola, L., Kessouri, F., Lefèvre, D., and Marsaleix, P.: Oxygen budget of the
916 north-western Mediterranean deep- convection region, *Biogeosciences*, 18, 937–960, <https://doi.org/10.5194/bg-18-937-2021>, 2021.

918 Ulses, C., Estournel, C., Marsaleix, P., Soetaert, K., Fourier, M., Coppola, L., Lefèvre, D., Touratier, F., Goyet, C.,
919 Guglielmi, V., Kessouri, F., Testor, P., and Durrieu De Madron, X.: Seasonal dynamics and annual budget of dissolved
920 inorganic carbon in the northwestern Mediterranean deep-convection region, *Biogeosciences*, 20, 4683–4710,
921 <https://doi.org/10.5194/bg-20-4683-2023>, 2023.

922 Velaoras, D., Krokos, G., Nittis, K., and Theocharis, A.: Dense intermediate water outflow from the Cretan Sea: A
923 salinity driven, recurrent phenomenon, connected to thermohaline circulation changes, *J. Geophys. Res. Oceans*, 119,
924 4797–4820, <https://doi.org/10.1002/2014JC009937>, 2014.

925 Wanninkhof, R. and McGillis, W. R.: A cubic relationship between air-sea CO₂ exchange and wind speed, *Geophys.*
926 *Res. Lett.*, 26, 1889–1892, <https://doi.org/10.1029/1999GL900363>, 1999.

927 Wolf, M. K., Hamme, R. C., Gilbert, D., Yashayaev, I., and Thierry, V.: Oxygen Saturation Surrounding Deep Water
928 Formation Events in the Labrador Sea From Argo-O₂ Data, *Glob. Biogeochem. Cycles*, 32, 635–653,
929 [:https://doi.org/10.1002/2017GB005829](https://doi.org/10.1002/2017GB005829), 2018.

930 Wu, Y., Zheng, Z., Chen, X., Huang, F., Liu, C., and Tang, D.: Amplified warming accelerates deoxygenation
931 in the Arctic Ocean, *Nat. Clim. Chang.*, 15, 859–865, <https://doi.org/10.1038/s41558-025-02376-0>, 2025.

932 Ziveri, P. and Grelaud, M.: Physical oceanography during Ángeles Alvariño cruise MedSeA2013,
933 <https://doi.org/10.1594/PANGAEA.846067>, 2015.